

# 1 Mapping out Min protein patterns in fully confined fluidic 2 chambers

3 Yaron Caspi<sup>1</sup> and Cees Dekker<sup>1</sup>

4 <sup>1</sup>Department of Bionanoscience, Kavli Institute of Nanoscience, Delft University of Technology, Van der  
5 Maasweg 9, 2629 HZ Delft, The Netherlands

## 6 Abstract

7 The bacterial Min protein system provides a major model system for studying reaction-diffusion processes in biology. Here we present  
8 the first *in vitro* study of the Min system in fully confined three-dimensional chambers that are lithography-defined, lipid-bilayer  
9 coated and isolated through pressure valves. We identify three typical dynamical behaviors that occur dependent on the geometrical  
10 chamber parameters: pole-to-pole oscillations, spiral rotations, and traveling waves. We establish the geometrical selection rules  
11 and show that, surprisingly, Min-protein spiral rotations govern the larger part of the geometrical phase diagram. Confinement  
12 as well as an elevated temperature reduce the characteristic wavelength of the Min patterns, although even for confined chambers  
13 with a bacterial-level viscosity, the patterns retain a  $\sim 5$  times larger wavelength than *in vivo*. Our results provide an essential  
14 experimental base for modeling of intracellular Min gradients in bacterial cell division as well as, more generally, for understanding  
15 pattern formation in reaction-diffusion systems.

## 16 Introduction

17 The Min protein system determines the localization of the division site in a wide range of bacterial cells [1, 2, 3, 4]. In  
18 *Escherichia coli* (*E. coli*), Min proteins dynamically oscillate from pole-to-pole on a typical time scale of about 1 minute  
19 [5, 6, 7]. Reaction-diffusion mechanisms were invoked in order to explain these oscillations [8], and as of today, the Min  
20 system is one of the most prominent examples of intracellular pattern formation in biology [9].

21 Three proteins participate in the *E. coli* Min oscillations: (i) MinD, an ATPase that can bind the plasma membrane  
22 through a short amphipathic peptide [10, 11] in a cooperative manner [12, 13]. Though it was commonly assumed that  
23 it binds the membrane only in its ATP-bound form [14, 15, 16], a recent work showed that MinD can also bind the  
24 membrane in the ADP-bound form [17]. (ii) MinE, a protein that is recruited to the membrane by MinD [18], upon which  
25 it induces MinD's ATPase activity causing MinD to be released from the membrane [19]. Subsequently, while diffusing in  
26 the cytosol, an exchange of ADP to ATP occurs, and the MinD proteins re-enter the cycle by rebinding the membrane.  
27 Several authors showed that MinE can persist on the membrane after MinD detachment [20, 21] or can even interact with  
28 the membrane by itself [22, 23, 17]. The exact contribution of this process to the overall Min dynamics remains unclear.  
29 Finally, (iii) MinC protein is also recruited to the membrane by MinD, but, due to overlap binding with MinE, is released  
30 from MinD after MinE binding [24, 25, 26]. While MinC is the sole member of the system that directly interacts with  
31 the division apparatus [27, 28, 29], it is believed to be only a passive hitchhiker that does not determine the dynamical  
32 behavior of the system. Thus, only MinD and MinE are needed in order to form dynamical pole-to-pole oscillations in *E.*  
33 *coli* cells.

34 A number of relevant properties of the Min system were identified when *E. coli* bacteria were perturbed from their  
35 native rod-shape form. When cells were grown as filaments, a dynamic series of Min bands with a characteristic length  
36 of  $\sim 8 \mu m$  was observed [5]. When the filamentous cells were grown at different temperatures, this length scale did not  
37 change but the temporal period of the oscillations decreased according to an Arrhenius law [30]. Likewise, in oval-shape  
38 cells, the Min system preferentially oscillated along the longest axis [31, 32]. Interestingly, while in round  $\Delta$ MreB cells,  
39 the Min oscillation occurred, in the majority of the cases, from one end of the cell to the other in a well-defined manner,  
40 in rounded rodA-amber-mutation cells, the oscillation direction moved chaotically from one spot along the membrane  
41 to another. A similar mode of chaotic oscillations was also observed when cells adopted aberrant shapes upon getting  
42 squeezed into slits smaller than their natural width [33]. In addition, when *E. coli* cells were mutated to form a Y shape,  
43 a sequence of oscillation nodes along the cell arms was observed that depended on the relative length of the Y shape  
44 arms [34]. These results show that the Min system can adapt to the cell geometry and modify its dynamical behavior  
45 accordingly. Indeed, in a recent example, Wu et al. sculpted *E. coli* cells into various rectangular and square shapes. They  
46 found that the Min system behavior was characterized by a typical length scale of  $3 - 6 \mu m$ . In addition, they showed  
47 that the choice for a particular Min pattern was governed by the symmetries of the cell shape, its aspect ratio, and its  
48 size. Consequentially, a variety of Min patterns were observed, including rotational, transversal, and longitudinal modes

49 [35].

50 In parallel with these cell-biology studies, *in vitro* reconstitution of the Min system on supported lipid membranes  
51 (SLB) significantly advanced the understanding of its dynamical mechanism [36]. On two-dimensional (2D) SLBs that are  
52 much larger than the typical length scale of the Min patterns, instead of oscillations, the Min proteins exhibit patterns  
53 that can be grouped into two classes: rotating spirals and traveling waves. In general, traveling waves were formed when  
54 bands that emanated from two counter-rotating spirals collided. Importantly, the wavelength of the traveling waves was  
55 very large, between 65 – 100  $\mu\text{m}$ , and depended on the ratio of MinD to MinE concentration. Thus, when the Min system  
56 is reconstituted *in vitro*, it exhibits a pattern-formation behavior with a typical spatial dimension that is about an order  
57 of magnitude larger than the one observed *in vivo*. Interestingly, when the Min system was reconstituted under limiting  
58 concentration conditions, unique patterns, in particular a bursting type, were observed [37]. It was suggested that these  
59 patterns might be more closely related to the behavior of the Min system *in vivo*.

60 One of the intriguing properties of the *in vitro* behavior of the Min system is its ability to adapt to geometrical patterns  
61 that are embedded in the SLB. For example, when rectangular patches of flat surface SLB were separated one from the  
62 other with gold barriers that were much larger than the characteristic size of the Min dynamics *in vitro* ( $\sim 100 \mu\text{m}$ ), Min  
63 waves propagated in a direction that depended on the aspect ratio of the patch [38]. Similarly, Min waves can be oriented  
64 within an SLB if parallel grooves are molded into the surface [39]. However, the geometry-selection rules that were found  
65 in these *in vitro* experiments do not correspond to the ones that were observed *in vivo* [35]. Recently, utilizing partly  
66 confined fabricated reaction chambers, Zieske and Schwille were able to reproduce Min pole-to-pole oscillations as well as  
67 double and triple-band standing waves, similar to the patterns observed in filamentous *E. coli* [40, 41]. Similarly, Zieske et  
68 al. showed that when grooves had a shape similar to that of dividing bacteria at the last division stage, the Min proteins  
69 stochastically distributed between the two sides of the grooves. This observation is similar to the way that Min proteins  
70 are distributed between the two progenies of an *E. coli* mother cell [42]. However, these *in vitro* Min oscillations were  
71 stable only when the groove width was much smaller than the *in vitro* wavelength of the waves. Since the geometrical  
72 selection rules of the Min patterns that were established in sculpted cells [35] do not coincide with the ones that were  
73 established for the *in vitro* grooves, the exact relation between the underlying mechanisms of these two phenomena of Min  
74 proteins remains unclear.

75 Recalling that the Min dynamics is a reaction-diffusion process, both the reaction and the diffusion parameters may  
76 control the behavior of the system *in vitro* as well as *in vivo*. Several experimental attempts have been made to study these

---

77 reaction-diffusion factors. For example, when the overall bulk diffusivity of the proteins was decreased by a factor of 10,  
78 the Min wavelength was, surprisingly, only marginally reduced [38]. In contrast, when the Min dynamics was studied on  
79 the outer side of giant unilamellar vesicles (GUVs), both the wavelength and wave velocity increased considerably relative  
80 to the behavior on an SLB [43]. It was suggested that the 4-fold increase in the diffusion of the Min protein on the GUVs  
81 membrane was responsible for this phenomenon. Concerning the reaction rates, by increasing the salt concentration or the  
82 ratio of anionic to natural phospholipids, Vecchiarelli et al. observed a reduction in the size of the Min bands [44], which  
83 they attributed to the different affinity of MinE to the membrane under these conditions. Similarly, Zieske and Schwille  
84 observed a decreased wavelength to a value of about  $25 \mu m$  by increasing the concentration of a negatively charged lipid,  
85 cardiolipin, in the SLB to an (unphysiologically high) molar ratio of 70% [41]. Note that even this reduced value is still  
86 much larger than the characteristic  $\sim 5 \mu m$  size scale measured *in vivo*.

87 Over the years, many mathematical models have been constructed for the Min system [45, 46, 47, 48, 49, 50]. Each  
88 of them postulated a somewhat different molecular mechanism and was able to reproduce several of the observed Min  
89 phenomena for certain values of the model's parameters. However, the ability to explain all Min behaviors and the  
90 robustness to changes in the parameters was less well considered. In particular, the ability to gap the *in vitro* and *in*  
91 *vivo* behavior of the system was not given much attention. Recently, Bonny et al. claimed that they were able to bridge  
92 this gulf [51]. However, they were only able to reproduce the *in vivo* oscillations and *in vitro* surface waves for reaction  
93 parameters that were different in both cases over several orders of magnitudes, and the experimental basis for this variation  
94 remained unclear. To date, the best Min model was developed by Halatek and Frey, based on a previous model by Huang  
95 and Wingreen [52, 53, 54]. This model is able to reproduce most of the *in vivo* experimental results over a wide range of  
96 geometries and conditions [35]. The ability of this model to reproduce the Min behavior *in vitro* was, however, not yet  
97 reported.

98 One reason for the lack of theoretical ability to reproduce all observed Min behaviors using a single set of parameters is  
99 the lack of comprehensive experimental results for the *in vitro* behavior of Min proteins under a wide range of geometrical  
100 confinements. First steps in this direction were taken by Zieske and Schwille [40, 41]. However, their compartment were  
101 only semi-confined and they probed the system behavior mainly for compartments that were much narrower than the  
102 typical Min wavelength, and hence, a full description of the geometrical selection rules for the Min system in confined  
103 chambers, and especially the relation between *in vitro* oscillations and *in vitro* traveling waves, is still missing.

104 Here, we studied the pattern formation behavior of MinD and MinE proteins inside fully 3D confined chambers,

under the aim to better understand the relations between different factors that determine the influence of geometry on the dynamics of the Min system *in vitro*. To obtain these chambers and encapsulate Min proteins inside them, we fabricated PDMS chips and coated all the chamber walls with SLB before injecting the Min proteins and spatially isolating the chambers from the rest of the chip through soft-lithography PDMS valves. We determine the Min patterns as a function of the geometrical factors of the chambers as well as of other factors such as temperature and viscosity, and compared these results to the one that are observed with flat SLB. We show that the rotational Min spirals can evolve to pole-to-pole oscillations if the dimensions of the confinement are reduced or to traveling waves if the dimensions of the confinement are increased. We provide a phase diagram that maps out the Min patterns over a wide range of geometrical parameters. In addition, we show that several parameters, including 3D confinement, medium viscosity and temperature can reduce the wavelength of traveling waves. Yet, all these parameters did not resolve the *in vitro/in vivo* dichotomy. Our comprehensive set of data, however, provides essential information that is needed in order to understand the molecular mechanism of the Min system, which underlies its essential pattern-formation abilities.

## Results

**Fabrication and preparation of spatially confined fluidic microchambers.** We fabricated microfluidic chips that are composed of two stacked PDMS layers (see Fig. 1(a)-(c) and Figure 1 - figure supplement 1 to Figure 1 - figure supplement 3). The bottom layer had structures of three different heights: (i) Rectangular chambers with height of  $\sim 2.4 \mu\text{m}$  and lateral dimensions ranging from  $10 \times 10 \mu\text{m}$  to  $60 \times 80 \mu\text{m}$  (blue part in Fig. 1(b)); (ii) Reservoir channels with height of  $\sim 30 \mu\text{m}$  and width of  $100 \mu\text{m}$  (red part in Fig. 1(b)); and (iii) thin connector channels with height of  $\sim 0.9 \mu\text{m}$  and width of  $\sim 0.9 \mu\text{m}$  (green part in Fig. 1(c)) that connects the reservoirs and the chambers. The upper layer of the device consisted of air-filled PDMS channels that were aligned directly above the reservoir channels and connected to a high-pressure argon line thus serving as pneumatic pressure valves [55]. Upon increasing the pressure of the air-filled channels in the upper layer, the ceiling of the lower layer (thickness  $\sim 20 \mu\text{m}$ ) deflected downward above the reservoir channels and closed the entrance to the connector lines. Using this design, we were able to spatially isolate the central PDMS chambers (blue in Fig. 1b) from the rest of the chip and to obtain totally isolated 3D confined volumes for studying the Min patterns.

We used the traditional method of rupture and spreading of small unilamellar vesicles (SUVs) for the formation of

an SLB onto all inner surfaces within our microfluidic device (SUVs composition 67% DOPC, 33% DOPG, supplemented with 0.03% TopFluor cardiolipin for fluorescent imaging) [56, 57]. After the device was flushed with SUVs and incubated for  $\sim 1$  h, a nice continuous SLB was formed on all the inner walls of the chambers (data not shown). This feature of our microchambers that are covered by an SLB from all sides is what distinguishes our approach from previous studies that reconstituted Min proteins in fabricated structures [36, 58, 38, 59, 40, 44, 41, 37]. Subsequently, the device was extensively washed in order to remove the residual SUVs. For several devices, we checked the formation of a fluid SLB using fluorescence recovery after photobleaching (data not shown); for other devices, we relied on the homogeneous fluorescence signal of the TopFluor cardiolipin. It was important, for each device, to check that the valves worked properly. As a quality control, we checked the functionality of the valves by operating them during the first stages of the washing process and observing the effect on the flow through the microchambers (see movie 1 and the Materials and Methods section). These results corroborated that upon closing the pressure valves, we obtained truly confined chambers in our microfluidic devices.

After the device was washed and the valves were tested for functionality, the chambers were filled with a solution containing MinD and MinE that we purified and labeled beforehand (MinE  $0.8 \mu M$ : MinE-Cy5  $0.2 \mu M$ : MinD  $0.9 \mu M$ : MinD-Cy3  $0.2 \mu M$ ), supplemented by ATP ( $5 mM$ ) and an ATP-regeneration system (see Materials and Methods). Subsequently, we closed the pressure valves and, after an incubation period of  $> 1 h$ , we recorded movies of the resulting dynamical behavior of the Min system.

**A variety of Min patterns in the microchambers.** We observed a rich set of dynamical phenomena for the spatio-temporal behavior of the Min proteins, and studied it in hundreds of confined chambers. In most of the cases, the Min proteins showed a defined pattern in each chamber that was stable for the duration of the movie acquisition ( $\sim 10$  minutes). Three primary dynamical behaviors stood out as the most prominent patterns; (i) pole-to-pole oscillations - where the Min proteins periodically move back and forth from one side of a structure to the other (see Fig. 1(d)); (ii) traveling waves - where the proteins move constantly from one side of a structure to the opposite side (see Fig. 1(e)); and (iii) spiral rotations - where the proteins constantly rotate in a spiral fashion within the microchamber (see Fig. 1(f)). As can be seen from Fig. 1(d)-(f), the typical time it took to reestablish the Min zone in these microchambers was  $1 - 5$  min.

For each chamber, we recorded a movie with the dynamical behavior of the Min system. To represent the temporal behavior in a specific chamber in the format of a still image, we adopted a quadrant scheme, see Fig. 2(a). Each quadrant is composed of: (top-left) a single frame from a movie of the dynamical pattern in this chamber; (bottom-left) an X-axis kymograph of the Min concentration along the horizontal chamber middle (red line in top-left image of Fig. 2(a));

159 (top-right) a Y-axis kymograph of the Min concentration along the vertical chamber middle (blue line in top-left image  
160 of Fig. 2(a)); and (lower-right) a temporal-standard-deviation (STD) image of the movie. In this scheme, each basic type  
161 of dynamical behavior such as oscillations, waves or spiral rotations has a distinct signature.

162 For example, for side-to-side oscillations (cf. Fig. 2(b)), the top-left representation of the quadrant may show a  
163 snapshot of the Min concentration at one side of the chamber. The Xt kymograph shows the movement of the Min  
164 proteins along the X-axis as they travel from the chamber middle to one side, then to the chamber middle, then to the  
165 other side of the chamber, and so on. This repetitive reappearing of Min proteins at the chamber middle results in oblique  
166 lines in the Xt kymograph that run from the Kymograph middle to both of its sides. In contrast, the reappearing of Min  
167 proteins in the middle of the chamber results in repetitive vertical lines in the Yt kymograph. Finally, the STD image  
168 shows the locations where the variations in the Min proteins are the largest, i.e., at the chamber sides in this example.

169 For a traveling wave (cf. Fig. 2(c)), the top-left single frame image in the quadrant representation can show, for  
170 example, two wave fronts propagating from the bottom right corner of the chamber to the opposite corner. The Xt and  
171 Yt kymographs for this case show a typical signature of continuous oblique lines that are formed as the Min proteins  
172 pass through the mid-lines of the chamber. The STD figure merits a comment. For an infinite-time movie of fully  
173 homogeneous waves, the STD figure of a traveling wave should have a uniform flat profile. For a finite-time recording of  
174 a wave propagation, the STD figure will, however, show a slightly monotonically decreasing profile.

175 For the rotational behavior (cf. Fig. 2(d)), the repetitive passage of the Min proteins along both the X-axis and the  
176 Y-axis chamber midlines results in oblique lines that run from the kymograph middle to its sides, for both the Xt and Yt  
177 kymographs. The STD image of Min protein rotation shows the focal point and a symmetric concentric gradient profile  
178 around it.

179 Fig. 2(e) represents a typical repertoire of the Min dynamical behaviors for the different geometries of the chambers.  
180 A corresponding composite movie 2 is also provided (very worthwhile to examine this movie, as it illustrates the intrinsic  
181 dynamic patterns particularly well). In addition, a zoom-in for the smaller chambers sizes is shown in Figure 2 - figure  
182 supplement 1. In this atlas of dynamical patterns, one can observe a variety of patterns, e.g., side-to-side oscillations in  
183 the  $30 \times 10 \mu m$  chamber, a traveling wave in the  $60 \times 50 \mu m$  chamber, and a spiral rotation in the  $40 \times 40 \mu m$  chamber.  
184 More complex dynamical patterns were also observed. For example, in chambers of size  $50 \times 10 \mu m$  and  $60 \times 10 \mu m$ ,  
185 instead of the most simple side-to-side oscillation, we observed a striped pattern, where the Min concentration oscillated  
186 back and forth from the center of the chamber to both sides (see Figure 2 - figure supplement 1). This is similar to what

187 has been observed in filamentous cells [5, 30], shaped long cells [35], and *in vitro* grooves [41]. Furthermore, in some cases  
188 we observed more than one rotational center within a single microchamber, a behavior that can be seen in the  $40 \times 20$   
189  $\mu m$ ,  $50 \times 20 \mu m$ ,  $60 \times 20$  and  $50 \times 30 \mu m$  chambers.

190 **Analysis of the Min pattern formation in confined microchambers.** We set out to quantify the relation  
191 between the dimensions of the chamber and the preferred dynamical behavior of the Min system. Altogether we analyzed  
192 the dynamical behavior of the Min proteins in 553 different chambers. For each chamber that was recorded, we identified to  
193 what class of dynamical behaviors the observed pattern conform to: (i) oscillations. (ii) traveling waves, or (iii) rotations.  
194 Cases with more than one rotational center in the chamber were tagged as rotations and cases of striped or side-to-side  
195 oscillations were tagged as oscillations. The large majority of observed patterns ( $> 95\%$ ) could be readily classified in  
196 these three categories. Naturally, there exist some borderline cases between the three types. For example, we observed  
197 that a rotational center of the Min proteins could propagate from one side of the chamber to the other. This behavior  
198 was grouped under the tag of traveling waves.

199 We thus analyzed the preferred dynamical behavior of the Min system in the chambers in terms of the geometrical  
200 parameters of the chambers such as the width ( $W$ ), length ( $L$ ), aspect ratio ( $L/W$ ), and area ( $L \times W$ ) of the chambers.  
201 The results are shown in Fig. 3(a)-(c) and Figure 3 - figure supplement 1(a). As can be seen, clear relations exist between  
202 the geometry of the chamber and the observed dynamical Min behavior. We note a few particular features: (i) Rotational  
203 patterns appear as the majority for chambers with small aspect ratio (Fig. 3(a)). As the chamber aspect ratio increases,  
204 the probability to obtain rotational behavior decreases, and for chambers with an aspect ratio larger than 2.8, we hardly  
205 observed rotational behavior in our chambers. (ii) Oscillatory behavior predominantly appears when the chamber width is  
206 small ( $\sim 10\mu m$ ) (Fig. 3(b)). (iii) Traveling waves mainly appear if the chamber length is relatively large (Fig. 3(c)), and  
207 their prevalence increases as the chamber length increases. Similarly, if the chamber area is relatively large the prevalence  
208 of obtaining a traveling waves increases (see. Figure 3 - figure supplement 1(a)). For these large areas, the confined  
209 chambers reflect the surface waves that were observed on unbound SLBs [36, 44]. The clear relation found between the  
210 chamber geometry and the dynamical Min patterns unambiguously proves that confinement sets the rules for Min pattern  
211 formation. It also supports the notion that the existence of the connector lines in our setup adds only second-order effects.  
212 Thus, by using the soft fabricated valves, we were able to extract and study, for the first time, the geometrical selection  
213 rules of the Min system in truly confined 3D structures *in vitro*.

214 **Phase Diagram of Min pattern in microchambers.** Having established a relation between the geometry of the

215 chambers and the spatio-temporal behavior of the Min system, we constructed the phase diagram of the Min patterns,  
216 see Fig. 4(a). In this phase diagram, each tile represents, in its color, the most prevalent Min behavior for the chambers  
217 with the designated specific dimensions. We restricted ourselves to cases for which we had data from at least 4 different  
218 chambers with this specific geometry; the typical number are 20 – 30 chambers per tile, see Figure 4 - figure supplement 1  
219 for the exact numbers. As can be seen from Fig. 4(a), the phase diagram is nicely separated into three different regions:  
220 (i) The majority pattern is rotations; (ii) oscillations are the most prevalent pattern in narrow chambers, in line with  
221 previous observation in semi-3D-confined structures [40, 41]; and (iii) as expected [36, 20], the most prevalent behavior  
222 for large and long chambers is that of traveling waves. The relative percentage of the oscillations, rotations and traveling  
223 waves is presented respectively in Fig. 4(b)-(d). The most striking, and unexpected, result of this study is that in fully  
224 confined 3D chambers, a large part of the phase diagram is occupied by rotational behavior, i.e., Min patterns that rotate  
225 around a fixed point in a spiral fashion. In other words, confining the Min system in 3D chambers mainly results in the  
226 formation of spiral waves. When the chambers becomes too narrow, these rotational centers are less stable, presumably  
227 due to reflection of the Min concentration front from the chamber boundaries, and oscillations are formed. Oscillations  
228 thus appear to be a derivative phenomenon that results from destabilization of spiral rotating patterns by the chamber  
229 walls. In the other extreme, for very large areas, the interaction between multiple rotational centers will equilibrate in  
230 such a way that the stable behavior becomes a traveling wave.

231 **Concentration of the Min proteins in the microchambers.** Theoretical models of the Min system rely on the  
232 concentration of the MinD and MinE proteins as an important control parameter. Determining the exact concentrations  
233 in the microchambers needs some considerations and is less trivial than it may appear to be at first glance. While Min  
234 proteins were injected at a well-defined concentration ( $1 \mu M$  MinE and  $1.08 \mu M$  MinD), the final concentration of the  
235 proteins in the chambers are higher than those introduced. The reason is that during the injection process, MinD molecules  
236 will bind the membrane, followed by MinE molecules, while proteins continue to flow into the chamber with the fresh  
237 bulk solution. This results in larger final concentration in steady state. We therefore measured the concentration of the  
238 final Min proteins inside our chambers using a green fluorescence protein (GFP) calibration. We measured the relative  
239 fluorescence of GFP, MinD-Cy3, and MinE-Cy5 in bulk using a fluorometer, yielding a calibration curve of intensity versus  
240 concentrations. Next, we injected the regular Min proteins mixture, which contains MinD-Cy3 and MinE-Cy5, together  
241 with GFP into the chambers, and measured the resulted fluorescence of the two labeled proteins verses that of GFP on  
242 a widefield microscope with a 20X objective. From that, one can infer the actual concentrations (see Figure 5 - figure

243 supplement 1(a)-(c) for the fluorometer calibration curves and the Materials and Methods section for the detailed derivation  
244 of Min proteins concentration in the chambers). Note that since GFP does not bind the membrane, its concentration in  
245 the microchambers is always known. Thus, it can be used as a calibration reference to estimate the concentration of the  
246 Min proteins, by comparing their relative fluorescence in the microchamber to the relative fluorescence for the case where  
247 there is no membrane binding (i.e. in the fluorometer cavity).

248 The concentration of the Min proteins was measured for 52 different chambers. As can be seen (Fig. 5 (a)), the actual  
249 concentration of the Min proteins in our chambers was significantly ( $\sim$ factor 5) higher than the value for the injected stock  
250 solution. Furthermore, a wide distribution is observed, particularly for MinE. Note that we did not observe a relation  
251 between the chamber size and the measured concentration of the Min proteins. From these measurements we concluded  
252 that the concentration of MinD in our chambers was  $4.5 \pm 0.5 \mu M$  (mean  $\pm$  SD), the concentration of MinE  $6 \pm 3 \mu M$ ,  
253 and the average ratio of  $[\text{MinE}]/[\text{MinD}]$  amounted to  $1.3 \pm 0.5$ .

254 **Wavelength of the Min waves in microchambers.** It is of interest to know if transforming the topology from  
255 surface 2D [36, 58, 20, 44] or semi 3D [40, 41] to a fully confined 3D topology will substantially change the wavelength  
256 of the traveling waves. This question is interesting since, as mentioned in the introduction, one of the open questions  
257 regarding the Min system relates to the differences between its spatial length scale *in vitro* verses *in vivo*. Mean and SD of  
258 the measured wavelength of 35 traveling-waves in confined chambers are shown in Fig. 6(a). We measured a wavelength  
259 of  $43 \pm 6 \mu m$  at room temperature. This value is significantly lower than the wavelength of  $78 \pm 12 \mu m$  ( $n = 30$ ) for  
260 traveling waves that we measured on 2D flat SLBs using the exact same protein and lipid composition of the SLB as was  
261 used in our microchambers experiments. This shows that the 3D full confinement of the Min system has a clear effect not  
262 only on the geometry-selection properties, but also on the characteristic length scale of the system.

263 Similarly, it is of interest to ask whether the confinement has any influence on the propagating velocity of the Min  
264 front. We compared the velocity of all different Min patterns in the chambers ( $n = 333$  chambers) to the propagation  
265 velocity of Min waves on the flat surfaces ( $n = 30$ ), see Fig. 6(b). While on flat SLB surfaces we measured  $v = 0.6 \pm 0.2$   
266  $\mu m/s$ , similar to previous measured values [20], inside the chambers we obtained a propagation velocity of  $0.3 \pm 0.1 \mu m/s$   
267 (while the propagation velocity was  $0.4 \pm 0.1 \mu m/s$  for waves only;  $n = 35$ ). The reduced wavelength inside the chambers  
268 was thus accompanied with a reduced velocity.

269 **Wavelength of the Min system in crowded environments.** We examined the effects of molecular crowding on  
270 the characteristics of the waves in our 3D confined chambers. Crowding the liquid environment can have multiple effects.

271 On the one hand, it increases the viscosity of the solution, thus, by Einstein's relation, reducing the diffusivity of the  
 272 proteins. This parameter is particularly important in reaction-diffusion processes, such as the Min dynamics, since the  
 273 diffusion rate of the fastest species determines the distance between two maxima of the pattern. On the other hand, the  
 274 use of a high concentration of molecular crowder (polymers or proteins) can have unintended side effects and influence the  
 275 stability and binding properties of the studied proteins themselves [60]. In order to maximize the viscosity of the solution  
 276 while minimizing the side effects, we employed a solution of 4% PEG 8000, 4% Ficol 400, and 4% BSA (all three commonly  
 277 used crowders). The measured viscosity of this solution is  $9.9 \pm 0.05$  cP, i.e., one order of magnitude larger than that of  
 278 water. Though the exact viscosity inside *E. coli* cells is unknown, this value is close to the estimated one [61]. The results  
 279 ( $n = 17$ ) for the wavelength and wave velocity of traveling Min waves in confined 3D chambers under these conditions are  
 280 shown in Fig. 6(a) and (b), see also Figure 6 - figure supplement 1 for examples of Min waves under viscous conditions.  
 281 Increasing the viscosity of the environment resulted in a factor 2 reduction of the wavelength from  $43 \pm 6$   $\mu\text{m}$  to  $23 \pm 4$   
 282  $\mu\text{m}$ . This reduction in the wavelength is comparable to the reduction in wavelength that was observed by Martos et al.  
 283 in the presence of 140 g/l Ficol [59]. Next to the reduction in the wavelength, we observed a very large decrease, of more  
 284 than one order of magnitude, in the wave velocity from  $0.3 \pm 0.1$   $\mu\text{m}/\text{s}$  to  $0.02 \pm 0.014$   $\mu\text{m}/\text{s}$ . Note that this substantial  
 285 decrease in the velocity is much larger than what was observed by Martos et al. and is probably related to the different  
 286 constellations of 2D surfaces (used by Martos et al.) in comparison to 3D confined microchambers (in this work).

287 **Dynamics of the Min system at elevated temperature.** The previous results showed that there are various ways  
 288 to modulate the velocity and characteristics length scale of the Min proteins, and prompted us to look for other means to  
 289 modulate these properties. We therefore studied the Min system properties in our chambers at an elevated temperature  
 290 of 37°C As can be seen in Fig. 3(d)-(g) and Fig. Figure 3 - figure supplement 1(b), the geometry selection properties of  
 291 the Min system at the elevated temperature of 37°C are very similar to those that were observed at room temperature  
 292 ( $n = 198$ ): (i) at low aspect ratio of the chambers ( $L/W$ ), the prevalence to obtain rotational patterns is high while it  
 293 decreases as the aspect ratio increases; (ii) oscillatory behavior is observed mainly for narrow chambers; (iii) traveling  
 294 waves become dominant for long and large chambers. The phase diagram at elevated temperature is shown in Fig. 4(e)  
 295 (a detailed analysis of the phase diagram is shown in Figure 4 - figure supplement 2). The overall picture remains the  
 296 same, although more scatter is apparent in the data.

297 The wavelength at the elevated temperature (see Fig. 6(a),  $n = 34$ ), shows only a small decrease relative to the  
 298 wavelength at room temperature, that is from  $43 \pm 6$   $\mu\text{m}$  to  $37 \pm 9$   $\mu\text{m}$  (two sample t-test with different variance= 0.001

at  $\beta = 0.05$ ). This contrasts the behavior of waves on flat 2D SLBs surfaces, for which we observed a much more profound effect (Fig. 6(a),  $n = 27$ ). In this case the wavelength reduced from  $78 \pm 12$  at room temperature to  $48 \pm 6 \mu\text{m}$  at  $37^\circ\text{C}$ . These data thus show that, in confined chambers, confinement is the major cause of the reduced wavelength, with the elevated temperature adding only a small further reduction in the characteristic spatial scale of the system.

Interestingly, we saw an increased, rather than a decreased, velocity of the Min proteins at high temperature. Results are shown in Fig. 6(b), measured from 162 chambers. At  $T = 37^\circ\text{C}$ , the velocity  $v = 0.5 \pm 0.3 \mu\text{m}/\text{s}$  (velocity for waves only  $v = 0.5 \pm 0.1 \mu\text{m}/\text{s}$ ;  $n = 34$ ). This compares to  $v = 1.4 \mu\text{m}/\text{s}$  (Fig. 6(b)) for waves propagating on flat SLBs surfaces. Thus, similar to the conditions *in vivo*, where the period of the oscillations is inversely correlated with the temperature [30], elevated temperature increases the velocity of the Min propagation *in vitro*, doubling from  $23^\circ\text{C}$  to  $37^\circ\text{C}$  both on 2D surfaces and in 3D confinement. However, in contrast to the *in vivo* behavior, the *in vitro* wavelength is also temperature dependent. Since the viscosity of the bulk media change only by a factor of 1.3 from  $23^\circ\text{C}$  to  $37^\circ\text{C}$ , we have to attribute these results to a change in one of the reaction parameters of the reaction-diffusion Min system. We can conclude that there are different ways to modulate the different dynamical characteristics (wavelength and velocity) of the Min system.

## Discussion

In this paper we report a comprehensive experimental data set of Min patterns in fully confined fluidic chambers that are internally coated on all surfaces with a supported lipid bilayer. The ability to obtain a detailed picture of the Min patterns *in vitro* is important for three reasons. First, the theoretical understanding of Min pattern *in vivo* is still incomplete, and *in vitro* studies with their exquisite control will help to resolve existing questions such as the origin of the symmetry-breaking mechanism. Second, the development of a comprehensive theoretical framework for the Min system behavior depends on the ability to experimentally compare the *in vivo* and the *in vitro* cases under well-defined conditions such as dimensionality and size. Third, applications that aim at utilizing the Min system for engineering complex behavior in synthetic cells and other man-made systems depend on the ability to fully control its behavior *in vitro*.

Previously, Min proteins were reconstituted *in vitro* [36, 58, 20, 38, 43, 44, 39, 59, 37], and Min oscillations were observed in fabricated microchambers [40, 41]. In the latter case, the microchambers had a half-open configuration (i.e., with a top surface not coated with SLB) with a limited width ( $\sim 10 \mu\text{m}$ ), a height of  $10 \mu\text{m}$ , and varying lengths leading to a range of aspect ratios (1.2 – 24). In our case, we studied the system for microchambers with a height of  $2.4 \mu\text{m}$ , a width

---

325 of  $10 - 60 \mu\text{m}$ , and a length of  $10 - 80 \mu\text{m}$ . We thus considerably expand previous experimental data since we mapped  
326 the Min behavior in a well-controlled manner over a section of the geometrical conditions where the microchambers have  
327 a much broader range of widths, while tightly restricting the height of the microchambers. The novelty of our approach  
328 can particularly be appreciated from the fact that, while previously no ordered patterns were observed in chambers wider  
329 than  $10 - 20 \mu\text{m}$  [40, 41], we observed a well-defined behavior of the system that was mapped into an ordered geometric  
330 phase diagram, as discussed below.

331 In this article, we have shown that total confinement of the Min system within 3D chambers leads to three main type  
332 of patterns: (i) rotational patterns in the form of spiral waves, which are the majority of the patterns found; (ii) periodic  
333 oscillations that occur mainly if the chamber width is small in comparison to the typical spatial length scale of the system  
334 *in vitro*; (iii) traveling waves that occur mainly if one of the dimensions of the chamber is larger than the typical spatial  
335 length scale of the system.

336 In our microchambers, rotational behavior in the form of one or multiple adjacent spiral waves thus contributes the  
337 largest fraction of the phase diagram. Spiral waves are common in various biological and chemical reaction-diffusion  
338 processes such as *Dictyostelium discoideum* aggregation, calcium variations in *Xenopus laevis* oocytes, and the famous  
339 Belousov-Zhabotinsky (BZ) reaction (see Reference [62] and references therein). They were also observed for the Min  
340 system on flat SLBs [36, 44]. For reaction-diffusion systems other than the Min system, various symmetry-breaking-  
341 mechanisms were invoked in order to explain this spiral behavior. For example, for the BZ reaction, spiral waves were  
342 attributed to a Hopf bifurcation mechanism [63]. In addition, it is well known that in nonlinear reaction-diffusion systems,  
343 several symmetry-breaking-mechanisms may coexist in different parts of the parameter phase space and, as result, a  
344 plethora of static or dynamic patterns can emerge [64]. Many times these patterns possess similar observable behavior, yet  
345 having different underlying symmetry-breaking-mechanisms. In light of this knowledge, it is well possible that *in vitro* Min  
346 patterns, in fact, emanate from a somehow different symmetry-breaking-mechanism than the Min oscillations in live cells  
347 despite the fact that the proteins are the same and the patterns share various similar characteristics with the *in vivo* case.  
348 In other words, in spite of the common belief that the main difference between the *in vivo* behavior of the Min system  
349 and its behavior *in vitro* is merely related to a different wavelength, possibly the symmetry-breaking-mechanisms are not  
350 exactly the same in both cases. The existence of spirals *in vitro* and their abundance in our confined microchambers,  
351 when compared to their absence from *in vivo* observations where pole-to-pole oscillations dominate [35], may be related  
352 to this.

---

353 Note that a complete understanding of a biochemical system depends on two complementary sources: a theoretical  
354 model that can predict the system behavior and detailed description of its behavior under as wide as possible experimental  
355 conditions. For a complex non-linear system, like the Min, it is relatively easy to construct a model that predicts the system  
356 behavior under a limited subset of the experimental data. This task becomes much harder, however, when experimental  
357 data exist for a wide range of conditions and system geometries. Such data thus help to restrict the class of possible  
358 theoretical models. In this report we provide such a detailed description of the *in vitro* behavior of the Min system in  
359 a wide section of the geometrical parameter space. Thus, our data restricts the possible classes of theoretical models  
360 that can explain the *in vitro* behavior of the Min system. In addition, since our microchambers height is relatively close  
361 to the actual diameter of a bacterial cell, our data further helps to restrict the possible models for symmetry-breaking  
362 mechanisms that can describe the system behavior *in vitro* as well as *in vivo*.

363 We observed that the spiral patterns were found to not be stable in narrow chambers that are smaller than or equal to  
364 the characteristic  $10\ \mu\text{m}$  length scale of spirals. We observe that pole-to-pole oscillations are established as the chamber  
365 walls restrict spirals to form. In other words, *in vitro* oscillations in fact appear to be a form of truncated spirals. This  
366 demonstrates how the interplay between geometrical confinement and the intrinsic spiral symmetry-breaking-mechanism  
367 of the Min system may produce distinct patterns. These data are the first to suggest that *in vitro* oscillations are truncated  
368 spirals, a fact that further shows the importance of studying the geometric phase diagram of the Min system, as was done  
369 here. Please note also that *in vivo*, spiral rotations were not observed [35]. Neither were they suggested as the origin of  
370 the symmetry-breaking mechanism in theoretical works. This serves as an additional note of caution for drawing a too  
371 simple correspondence between oscillatory patterns that are observed *in vitro* and those observed *in vivo*.

372 Our findings are further corroborated by comparing the nature of oscillations *in vitro* to those that are formed *in vivo*.  
373 To study this difference, we collected movies of *in vivo* oscillations (see supplementary file 1 and movie 3). By comparing  
374 the kymographs in both cases (Fig. 2(e), Figure 2 - figure supplement 1 and supplementary file 1(e)-(g)), one can clearly  
375 see the distinctly different behavior in these two cases. *In vivo*, the pole-to-pole oscillations amount to the establishment  
376 of polar zone that is replaced by a second polar zone near the opposite pole within a short time scale. In contrast to this,  
377 *in vitro* oscillations are more akin to a traveling wave that propagates toward one pole, whereupon it is then replaced  
378 by a wave that is established close to the chamber middle and propagates toward the opposite pole (we acknowledge  
379 the anonymous referee 3 for pointing out this difference). Similar behavior was also observed in *in vitro* oscillations of  
380 other reconstitution work [41]. This may also be the reason why steep *in vitro* Min gradients that would restrict FtsZ

381 localization to a single ring could not have been established. Note that *in vitro* we report the MinE signal while *in vivo*  
382 we imaged MinD (as the MinE signal was low in this strain). Essentially this does not alter the conclusion that is drawn  
383 here since in this strain the MinE signal merely follows the MinD signal (see [65]).

384 Why do traveling waves form the majority pattern in very large chambers while spirals are less abundant? *In vivo*,  
385 Min waves are hardly detected. Shih et al. reported the formation of transient Min waves in *E. coli* cells harboring the  
386 MinE<sup>D45A/V49A</sup> mutation that prevents the dimerization of MinE [66]. Recently, Bonny et al. also reported traveling  
387 waves in filamentous cells, but the abundance of this phenomenon was not reported [51]. In this last case, the Min operon  
388 was induced at a saturating concentration and thus the concentration of MinDE was probably much higher than in the  
389 native case for *E. coli* [67]. Finally, *in vivo* traveling waves were also observed in a small minority of filamentous cells,  
390 even if the Min operon is not over-induced and when the Min proteins do not harbor any mutations (see supplementary  
391 file 1(d) and movie 3). Note that in all these cases, the *in vivo* traveling waves represent a form of abnormal behavior  
392 which occurs if the MinE function is impaired or in other anomalous cases. This contrasts to the *in vitro* case, where  
393 traveling waves can be a generic feature of the Min system. In contrast to sporadic reports of Min waves *in vivo*, waves  
394 are almost always detected in *in vitro* assays on 2D SLBs. Two reasons are responsible for this observation. First, on  
395 flat 2D SLBs the spirals waves are not confined and hence waves that emanate from one center can travel long distance  
396 and interfere with waves that emanate from a second spiral center to form traveling waves. In our chambers, when their  
397 area became large, the intrinsic Min pattern formation mechanism and the reflection from the chambers walls resulted in  
398 the annihilation of spiral centers and the establishment of traveling waves, similar to the 2D case where boundaries are  
399 absent. The second reason for the formation of traveling waves is probably related to the concentration of the proteins in  
400 the *in vitro* assay. In a typical *in vitro* assay, one usually controls the bulk concentration of the proteins as the supply  
401 material. However, due to the small surface-to-volume ratio in typical *in vitro* assays, the actual concentration of the  
402 proteins on the membrane and the replenished reservoir of new Min proteins is higher than *in vivo* (cf. the above section  
403 on Min concentration in the microchambers). In fact, due to the experimental protocols employed, this observation is  
404 also correct for previous reconstitutions of the Min system in grooves [41], as well as for published *in vitro* Min system  
405 flow assays [44, 58]. This situation is qualitatively different from the *in vivo* case where, during the formation of polar  
406 zone or a Min band, most of the MinD proteins are recruited to the membrane and the cytosolic concentration thus drops  
407 to a low value. Indeed, in a very recent publication, Vecchiarelli et al. suggested that *in vitro* waves spirals are related  
408 to high concentration of the Min proteins while reconstituting the Min system under limiting concentration conditions

---

409 resulted in a dynamical series of Min bursts that are reminiscent of the behavior in cells [37]. Vecchiarelli et al. further  
410 checked the behavior of the Min proteins when MinE was replaced by a membrane-binding deficient mutant MinE<sup>11-88</sup>,  
411 and observed that in this case, Min waves were supported at high protein concentration, but bursting dynamics were  
412 absent. This observation was consistent with the one of Zieske et al. [41] where oscillations were not observed with  
413 a similar mutant MinE( $\Delta 3 - 8$ ). Thus, it seems that the interrelations between several factors determine the pattern  
414 formation mechanism in vitro: the surface-to-volume ratio, the protein concentration, the confinement, and the binding  
415 of MinE to the membrane. Our results, with the relatively high Min protein concentration that we measured, support  
416 their conclusions. The fact that we fully confined the Min system in 3D chambers with a relatively small height enabled  
417 us to look on the behavior of the system in conditions with a surface-to-volume ratio that is much larger than previously  
418 studied. Combined with our measurements of the total Min protein concentration in the chambers, our results set a lower  
419 limit for the protein concentration that still reproduces traveling waves, rotational spirals, or oscillations under these  
420 geometric conditions. It will be interesting to check if current models of the Min system that reproduce *in vivo* behavior  
421 will also be able to reproduce traveling waves by simply increasing the proteins concentrations. Indeed, Bonny et al. were  
422 able to show traveling waves in their theoretical system by increasing the Min concentration by 63% or by increasing the  
423 MinE to MinD ratio [51]. In our geometrical analysis of Min patterns selection, we showed that in chambers with high  
424 surface-to-volume ratio, and a high Min proteins concentration, the cumulative effect of annihilation of multiple spirals  
425 and of the reflection from the walls can result in the formation of traveling waves.

426 A related question regards the Min wavelength. We have observed a reduction in the Min wavelength by a factor of  
427 two in our microchambers relative to the case of 2D flat SLB. Taking a reaction-diffusion point-of-view, this observation  
428 can be explained in two ways. First, the lateral confinement by itself may be responsible for choosing dynamical modes  
429 of the system with a smaller wavelength. Second, the height reduction could change the balance between the reservoir  
430 of the free Min proteins in solution relative to the bound ones. Indeed, based on their model, Halatek and Frey recently  
431 suggested, that reducing the volume of Min proteins above the surface will drive the typical wavelength of the system to  
432 lower values (personal communication). Similarly, it was shown theoretically by Thalmeier et al. [54] that even in the  
433 absence of MinE, *Arabidopsis thaliana* MinD can form an intracellular gradient just based on the relations between the  
434 bulk diffusion and nucleotide exchange rates, but only in highly confined spaces. Thus, our observation that reducing the  
435 height of the chamber is accompanied by a reduction of both the wavelength and the wave velocity further stresses the  
436 value of our approach of studying the Min behavior in 3D confined spaces with a high surface-to-volume ratio. We note,

437 however, that our chambers are  $2.4 \mu\text{m}$  high, not too much larger than the  $1 \mu\text{m}$  diameter of an *E. coli* bacterium, and  
438 yet, we measured a wavelength that is an order of magnitude larger than the characteristic length scale observed *in vivo*.

439 We have shown that two factors can lower the wavelength further. First, the Min wavelength decreased by a factor of 2  
440 when the viscosity of the medium was raised to  $10 cP$ , i.e., similar to that of cells and ten times larger than a regular buffer.  
441 Still, even at this high viscosity, the wavelength was larger by a factor of  $\sim 5$  from the one measured *in vivo*. In addition,  
442 the reduction in wavelength was accompanied by a very large reduction in the wave propagation velocity. Note that the  
443 measured velocity in the highly viscous media was similar or even smaller than the one measured *in vivo* [68] (see also  
444 the supporting information in reference [51]). It is thus unlikely that additional increases in viscosity can bring both the  
445 characteristic length scale and the propagation velocity of the system *in vitro* to the *in vivo* values. Interestingly, unlike  
446 the situation in unconfined 2D reconstitution of the Min proteins [59], in microchambers with a high surface-to-volume  
447 ratio, the period of the Min wave (i.e., wavelength/velocity) was not constant but was reduced by a factor of about 8.

448 Second, we showed that increasing the temperature also reduced the wavelength. The effect of the temperature on the  
449 characteristic wavelength was much larger for the Min waves on flat SLBs than in the 3D confined chambers. Since the  
450 diffusion rate does not change substantially between room temperature and  $37^\circ\text{C}$  (only a factor of 1.3, by the Einstein's  
451 relation), the temperature effect in the 2D surface case is most likely the result of a change in one of the reaction  
452 parameters, most probably the ATP hydrolysis rate. This situation is different in the microchambers. Our observations  
453 suggest that the main *in vitro* determinant of the wavelength at elevated temperature in confined spaces is the geometrical  
454 confinement itself. In other word, geometrical confinement forces the system to choose a reaction-diffusion mode with a  
455 reduced wavelength which can only marginally be tuned further by increasing the temperature. Thus, in highly confined  
456 spaces the effect of temperature on the characteristic scale of the Min system is largely diminished, and is accounted by  
457 the small increase in diffusion rate. This fact can explain the previous *in vivo* results where no temperature dependence  
458 for the wavelength was detected [30]. It should be noted that the reduced length scale was accompanied by an increase,  
459 rather than a decrease, of the wave velocity. This observation is in line with the *in vivo* case where the oscillation period  
460 was smaller at high temperature. Our results points out that the dynamical characteristics of the Min system contain  
461 several decoupled parameters, such as wavelength and velocity that can be tuned in opposite directions. It is thus essential  
462 to study their action in the context of 3D confined spaces with a high surface-to-volume ratio.

463 The symmetry-breaking mechanism of the Min pattern formation depends on a combination of all its dynamical  
464 parameters. We have shown that dynamical aspects of the system can be tuned in at least three different ways: by

465 confinement, by changing the temperature, and by reducing the bulk viscosity. Yet, since in our 3D confined structures,  
466 even at elevated temperature or with high viscous media, the *in vitro* Min behavior did not quantitatively reproduce the  
467 *in vivo* one, probably a change of yet another dynamical parameter is necessary. This can be a simple thing like a change  
468 in the concentration of one of the Min proteins [37] or a change in one of the reaction rates. It is also possible that  
469 yet another physical or biological mechanism contributes to the different symmetry breaking in both cases. Biochemical  
470 assays have shown intricate effects of the Min system on the membrane organization in the *in vivo* context. For example,  
471 MinD increased the order of the lipids and decreased their mobility in inverted inner *E. coli* membranes that contained  
472 integral proteins more than it does in synthetic vesicles that are purely lipidic [69]. Similarly, the Min system affects the  
473 association of inner-membrane peripheral proteins and interacts with some of them directly [70]. It is thus possible that a  
474 yet unidentified protein species is needed in order to reproduce the *in vivo* geometrical selection rules of the Min system  
475 in an *in vitro* environment.

476 To sum up, we have studied the geometry selection rules of the Min system in 3D fully confined chambers. We found  
477 three main patterns in these confined chambers: spiral rotations, oscillations and traveling waves. Spiral behaviors were  
478 the most abundant ones in a large part of the phase diagram and we suggest that both traveling waves and oscillations  
479 result from interrelation between the spiral symmetry-breaking mechanism and the effects of confinement.

## 480 **Materials and Methods**

### 481 **Materials**

482 1,2-dioleoyl-sn-glycero-3-phosphocholine (DOPC), 1,2-dielaidoyl-sn-glycero-3-phospho-(1'-rac-glycerol) (DOPG) and *E.*  
483 *coli* polar lipid extract were purchased from Avanti polar lipids. Tris was purchased from Promega. Potassium chlo-  
484 ride and imidazole were purchased from Merck. Silicon wafers were from universitywafers.com. RTV 615 PDMS was  
485 purchased from Momentive. Nitric acid was from Merck. Cy3-NHS and Cy5-maleimide dyes were purchased from GE  
486 Healthcare. Phosphoenolpyruvic acid (PEP) was from Alfa Aesar. All other materials were from Sigma-Aldrich unless  
487 otherwise stated.

## 488 Fabrication of structures on silicon wafers

489 To fabricate the lower layer of the chip, which consists of structures with three different heights, a silicon wafer was  
490 processed in three different steps. First, a 4'' wafer was cleaned with a nitric acid for 10 minutes under sonication, washed  
491 with water and then dried. PMMA 495K 8A (MicroChem) was spincoated on the wafer at 500 rpm for 5 seconds and  
492 then at 3000 rpm for additional 55 seconds. Next, the wafer was baked for 1 hour at 180°C and the chambers pattern  
493 that was designed using Klayout (RRID:SCR\_014644) was written on the PMMA layer using a Vistec EBPG 5000+  
494 (acceleration voltage 100 kV, aperture 400  $\mu\text{m}$ , dose of 800  $\mu\text{C}/\text{cm}^2$  and a resolution of 100 nm). Altogether 9 similar  
495 chamber structures were written on the wafer. The written PMMA layer was developed in MIBK: isopropanol (1 : 3) for 9  
496 minutes, was washed for 30 second in isopropanol (IPA) and the wafer was spin dried. A Bosch deep reactive-ion etching  
497 process, with an inductive coupled plasma (ICP) reactive-ion etcher (Adixen AMS 100 I-speeder), was used to etch the  
498 structures into the silicon wafer. The process consisted of alternate etching (sulfur hexafluoride,  $\text{SF}_6$ ) and passivation  
499 (octafluorocyclobutane,  $\text{C}_4\text{F}_8$ ) cycles. During the process the pressure was kept around 0.04 mbar, the temperature of  
500 the wafer was kept at 10°C, while the plasma temperature was 200°C. The sample holder was held at 200 mm from the  
501 plasma source. The etching step involved 200 sccm  $\text{SF}_6$  for 7 sec with the ICP power set to 2,000 W without a bias on  
502 the wafer itself. The passivation step was done with 80 sccm  $\text{C}_4\text{F}_8$  for 3 sec with the ICP power set to 2,000 W and the  
503 bias power on the wafer alternate with a low frequency: 80 W, for 10 ms, and 0 W for 90 ms. Total etching time was 34  
504 seconds. After etching, the wafer was cleaned with Nitric acid for 10 minutes with sonication.

505 Next, the connector lines were fabricated on the same wafer via similar steps with the following small modifications.  
506 Spincoating of PMMA was done at 3000 rpm in the second step. Baking was done for only 45 minutes. The dose was  
507 742  $\mu\text{C}/\text{cm}^2$  and the resolution was 15 nm. Development was done for 3 minutes. After development the PMMA was  
508 descummed on Tepla machine at 0.6 mbar at 300 W with 100 sccm  $\text{O}_2$  for 1.5 minutes. Dry etching was done on the same  
509 Adixen AMS 100 I-speeder machine. The first step was the same as previously described only that the  $\text{SF}_6$  step lasted  
510 2.4 second and the passivation step lasted 1 second. The total etching time was 10 seconds. Next, another dry etching  
511 step was applied, this time the ICP power was set to 250 W, the bias power was 20 W, the source-target distance was  
512 240 mm, pressure was kept around 0.04 mbar and the temperature was kept at 10°C. The gas combinations was  $\text{SF}_6$  200  
513 sccm, Ar 100 sccm and  $\text{O}_2$  100 sccm. Total etching time was 5 minutes. The wafer was then cleaned in the Adixen AMS  
514 100 I-speeder machine at a pressure of 0.04 mbar, ICP power of 2500 W with a biased power of 60 W, a source-target

515 distance of 200 mm and a temperature of 10°C, using a  $O_2$  gas at 200 sccm for 5 minutes. The wafer was finally cleaned  
516 in Acetone at 45°C for 10 minutes and in fuming nitric acid for 10 minutes with sonication.

517 The reservoirs were fabricated similar to the chambers with the following modifications: the e-beam writing resolution  
518 was 150 nm with a dose of 889  $\mu C/cm^2$ . Development was done for 12 minutes. Etching was done for 320 seconds.  
519 Final cleaning was done at 45°C for 10 minutes in acetone following by cleaning step in nitric acid for 10 minutes with  
520 sonication.

521 To fabricate the upper valves, a 4'' wafer was cleaned with a nitric acid for 10 minutes under sonication, washed with  
522 water and then dried. Next, a thin layer of hexamethyldisilazane (BASF SE) was spincoated (1,000 rpm for 1 min) and  
523 baked at 200°C for 2 minutes. The negative e-beam resist NEB22A (Sumitomo Chemical Co., Ltd) was spin-coated (1,000  
524 rpm for 1 min) and the wafer was baked at 110°C for 3 minutes. The structures were written similar to the chambers that  
525 were described above with a resolution of 100 nm and a dose of 20  $\mu C/cm^2$ . The structures were immediately developed  
526 in MF322 (Dow Chemical Company) for 45 seconds following by a moderate development with MF322:water (1 : 9) for  
527 15 seconds and a wash in water for additional 15 seconds. Etching was done using the same reactive ion etching process  
528 that is described above for 130 seconds. Finally, the wafer was cleaned with nitric acid for 10 minutes under sonication.

529 After fabrication of both wafers (the one with the lower layer and the one with the upper layer), they both were  
530 rendered hydrophobic by placing the wafers for at least 12 hours in a desiccator at a pressure of  $\sim 0.6$  mbar together with  
531 30  $\mu l$  of (tridecafluoro-1,1,2,2-tetrahydrooctyl) trichlorosilane (abcr GmbH & Co.). This treatment forms a hydrophobic  
532 monolayer on the wafers surface.

533 To study Min patterns on 2D surfaces we fabricated PDMS flow cells with lateral dimension of  $6.325 \times 2 \text{ mm}^2$ .  
534 First, a silicon wafer was cleaned for 10 min in nitric acid under sonication. Next, a thin layer of hexamethyldisilazane  
535 was spincoated (1,000 rpm for 1 min) and baked at 200°C for 2 minutes, following by spincoating of AZ 5214 resist  
536 (Microchemicals GmbH) at 1000 rpm and baking step at 105°C for 4 min. The wafer was then exposed on EVG 620 mask  
537 aligner (EVG) through a polyester film photomask (JD photo) and was developed with MF321 (Dow Chemical Company)  
538 for 4 min following by a washing step in water for 30 *sec*. Next, the wafer was baked for 10 min at 180°C and was etched  
539 similar to the chambers pattern with the slight modification that the etching time was 60 min. The depth of the flow  
540 channels was 137  $\mu m$ . Finally, the wafer was cleaned using nitric acid for 10 min under sonication and was rendered  
541 hydrophobic as described above.

## 542 **Formation of the PDMS chips**

543 Since PMMA is a positive resist, the surface of the lower wafer contained grooves that are identical to the ones we like  
544 to have on the PDMS chip. In order to get a PDMS layer where the reservoirs, chambers and side channels are grooved  
545 inwards we have used the method of double replication of the structures with PDMS. First, 30 g of RTV615 at a volume  
546 ratio of 5 : 1 base:crosslinker were poured on the lower layer wafer and were baked for 4 hours at 60°C following by a  
547 baking step for another 4 hours at 120°C. Next, 9 different chips (20 × 20 mm) were cut from the PDMS mold, and  
548 served as masters for the second step replication. These masters were treated with (tridecafluoro-1,1,2,2-tetrahydrooctyl)  
549 trichlorosilane in the same way as is described above. To form a thin PDMS lower layer containing all the desired  
550 structures, RTV615 at a mass ratio of 5 : 1 base:crosslinker was spincoated separately on each master (500 rpm for 30  
551 seconds followed by a step at 1400 rpm for 60 seconds). The PDMS masters with the spincoated PDMS layer were then  
552 baked at 60°C for 45 – 60 minutes.

553 Glass coverslips (22 × 22 mm, VWR, thickness no. 1.5) were cleaned by sonication in acetone for 30 minutes following  
554 by a sonication step in isopropanol (IPA) for 30 minutes and a final wash in MiliQ water. The coverslips and the top  
555 layer of the spincoated PDMS were plasma activated for 12 seconds in a plasma machine (Plasma PREEN I, plasmatic  
556 system Inc.) with a flow of 1 SCFH O<sub>2</sub>. A coverslip was bound on top of each spincoated PDMS layer and was baked  
557 for 10 minutes at 60°C. The coverslip-bound chips were immersed in methanol overnight. Finally, the lower PDMS layers  
558 bound to the corresponding coverslips were peeled off the PDMS masters, dried and kept separately in a plastic box.

559 To form the PDMS layer that separates the upper and lower layers, 5 – 10 g of RTV615 was poured on a flat 4" wafer  
560 that was treated with (tridecafluoro-1,1,2,2-tetrahydrooctyl) trichlorosilane as was described above, and the PDMS was  
561 spincoated (500 rpm for 30 seconds followed by a step at 2000 rpm for 120 seconds) to form a thin layer that was baked  
562 at 60°C for 1 hour.

563 To form the upper PDMS layer, 30 g of RTV615 at a mass ratio of 5 : 1 base:crosslinker were poured on the upper  
564 layer wafer baked at 60°C for 45 – 60 minutes, and 20 × 20 mm pieces were cut from PDMS mass.

565 Next, the upper PDMS layer pieces and the PDMS separation layer were plasma activated for 12 seconds at Plasma  
566 PREEN I machine with 1 SCFH O<sub>2</sub>, bound one to the other and were baked at 60°C for 10 minutes.

567 Before each experiment, the upper PDMS layer bound to the separation PDMS layer was peeled off the flat silicon  
568 wafer, holes were punched and both the peeled piece and a lower layer coverslip-bound chip were plasma activated for 12

seconds with a Plasma PREEN I machine supplemented with a flow of 1 SCFH  $O_2$ , and aligned manually one on top of the other using a home-build alignment machine build on a IX71 Olympus microscope that was equipped with a 4X objective (UPIanFLN, N.A. 0.13). Finally, the two parts were bound to each other and were baked at 80°C for 10 minutes.

For preparing the PDMS chips of the large flow cells that were used for studying the Min dynamics on 2D surfaces, RTV615 at a mass ratio of 10 : 1 base:crosslinker, was mixed, poured on the silicon wafer master and baked for 1 – 2 h at 80°C. Subsequently, the PDMS was peeled from the silicon wafer, a PDMS chip (20 × 20 mm) was cut, holes were punched and both the chip and a coverslip (that was previously cleaned in acetone and isopropanol as described before) were activated for 12 seconds with a Plasma PREEN I machine supplemented with a flow of 1 SCFH  $O_2$ . Finally, the PDMS chip was bound to the coverslip and was baked for 10 min at 80°C.

### Purification of Min proteins

Purification of MinD and MinE was done as described before [36] with slight modification. Briefly, BL21(DE3) containing pET28a with either His-MinD or His-MinE were grown in the presence of 50  $\mu M$  kanamycin in LB media to an O.D. of  $\sim 0.6 - 0.8$  at 37°C and 180 rpm shaking. Next, the expression of the Min proteins was induced with 1 mM of IPTG and the cells were grown overnight at 18°C with 180 rpm shaking. The cell were then harvested by centrifugation at 4500 g for 30 minutes, washed with buffer A (50 mM sodium phosphate pH 8.0 at 4°C, 300 mM NaCl), and then were resuspended in a lysis Buffer (buffer A supplemented with 10 mM imidazole, 5 mM TCEP (tris(2-carboxyethyl)phosphine), a complete protease inhibitor (Roche) and 100 mM ADP for the MinD case only). Cells were lysed in cell disrupter machine at 15,000 PSI and the lysate was cleared by centrifugation at 37500 g for 1 hour. The supernatant was loaded on a 5 ml HisTrap column (GE Healthcare) on an AKTA machine (GE Healthcare), and the column was washed once with lysis buffer supplemented with 10% glycerol. Next, the column was washed with the same buffer + 20 mM imidazole +10% glycerol and with the same buffer+ 50 mM imidazole+10% glycerol. MinE was eluted with 250 mM imidazole and MinD with 160 mM imidazole. Min proteins fractions were collected, concentrated with amicon ultra 10 kDa (Merck Millipore) and further purified on Sephacryl *S* – 300 HR 16/60 column on an AKTA machine (GE Healthcare) using a storage buffer (50 mM Hepes pH 7.25 at 4°C, 150 mM KCl, 10% V/V glycerol, 0.1 mM EDTA pH 7.4 and 80  $\mu M$  of ADP for the MinD case).

Protein concentration was measured using a QuantiPro<sup>TM</sup> BCA assay kit (Sigma-Aldrich). The ATPase activity of MinD was measured by detecting the reduction in the NADH absorption line at 340 nm. For the activity assay, 100  $\mu l$  of

596 solution, containing MinD ( $1 - 5 \mu M$ ) was incubated together with MinE ( $1 - 5 \mu M$ ), *E. coli* polar-lipid SUVs ( $1 mg/ml$ ),  
597 Pyruvate kinase (PK) ( $0.02 mg/ml$ ), ATP ( $5 \mu M$ ), Phospho(enol)pyruvic acid (PEP,  $5 \mu M$ ) at  $37^\circ C$ . Negative control  
598 assays without MinE, without the liposomes, or without the MinD, were similarly prepared and handled. At specific  
599 times (every 40 to 60 minutes),  $4 \mu l$  fractions of the activity assay or the control reactions were removed and added to  
600  $36 \mu l$  containing PEP ( $2.1 mM$ ), NADH ( $0.22 \mu M$ ) and a solution of Lactate dehydrogenase/PK (Sigma-Aldrich, 22 U  
601 of each component). Next, the mixed solutions were incubated at  $37$  degrees for 10 min and then moved to ice. Finally,  
602 the absorption at  $340 nm$  was measured using a nanodrop machine (Data not shown). We used NHS-Cy3 to label MinD  
603 and Maleimide-Cy5 to label MinE according to the manufacturer procedure (GE Healthcare). The degree of labeling was  
604  $\frac{Cy3}{MinD-Lysine} = 0.88$ ,  $\frac{Cy5}{MinE-Cysteine} = 0.45$ .

### 605 Preparation of Small Unilamellar Vesicles

606 Small unilamellar vesicles (SUVs) were prepared through the common method of thin film hydration. Briefly, lipids in  
607 the selected molar ratio dissolved in chloroform were mixed in a round shaped flask (either *E. coli* polar lipid extract  
608 or 67 : 33 DOPC:DOPG supplemented with 0.03 of TopFluor Cardiolipin, except for measuring proteins concentration  
609 where the TopFluor Cardiolipin was not added). The chloroform was evaporated using a nitrogen stream and further  
610 by incubation in a desiccator for at least 2 hours at a pressure of  $\sim 1$  mbar. Next SUV buffer (10 mM Tris pH 7.45 at  
611  $21^\circ C$ , 150 mM KCl) was added to a final concentration of  $5 mg/ml$  and were shaken at 250 rpm until all the lipid film  
612 completely hydrated. Next, the solution was sonicated at  $36^\circ C$  for  $\sim 30$  min and was extruded through 30 nm filter 21  
613 times. Finally, the SUVs were frozen in liquid nitrogen and stored at  $-80^\circ C$ .

### 614 Observation of Min Patterns

615 Min protein were observed on a commercial Olympus IX81 microscope equipped with a 60X objective (PlanApoN TIRFM  
616 UIS 2, NA 1.45, oil immersion) or with a 20X objective (UPlansApo, NA 0.85, oil immersion), a USHIO USH-1030L  
617 mercury lamp, a Mad City lab Micro-drive stage, an Uniblitz VMM-T1 shutter drive and a Hamamatsu C4742-95 12ERG  
618 camera. Microscope was controlled via the Micro-Manager program [71], and the stage was controlled via a self-written  
619 program in Labview. For high-temperature experiments, we used a Julabo F12 water-circulating bath that was connected  
620 to a custom-designed heating chamber and an objective heater (Live cell instruments, chamslide.com).

621 In a typical chamber experiment, we first flushed SUVs into the device at a concentration of  $2.5 mg/ml$  in SUV buffer.

622 The vesicles were incubated inside the device at 37°C for 1 hour. Next, the chip was washed with a Harvard apparatus  
623 11 plus pump using a Min buffer (25 mM Tris pH 7.45 at 21°C, 150 mM KCl, 5 mM MgCl<sub>2</sub>) for about 1 hour at a flow  
624 rate of 75 – 150  $\mu$ l/h. For room-temperature experiments in the chambers, we used a lipid composition of DOPC:DOPG  
625 (67:33) supplanted with 0.03% TopFluor Cardioliolipin. For the elevated temperature experiments in the chambers, we used  
626 *E. coli* total lipids extract supplemented with 0.03% TopFluor Cardioliolipin.

627 After the chambers were extensively washed, 10 – 50  $\mu$ l of Min buffer containing (unless otherwise mentioned): 1.1  
628  $\mu$ M MinD (either alone or in most of the cases in total divided between 0.9  $\mu$ M MinD plus 0.2  $\mu$ M MinD-Cy3), 0.8  $\mu$ M  
629 MinE, 0.2  $\mu$ M MinE-Cy5, 5 mM ATP (magnesium salt), 4 mM PEP, and 10  $\mu$ g/ml PK, was injected into the device  
630 and the inlet and outlet were blocked using a sellotape. Next, the device was placed under the microscope. After assuring  
631 that pattern started to form in the chambers ( $\sim$  10 min after injection), the valves were closed by applying a pressure of  
632 2 – 3 bars from an argon gas cylinder and the device was incubated for additional of  $\sim$  1 h. Finally, the device was scanned  
633 and movies lasting  $\sim$  10 minutes were recorded. Typically, the frame rate was 0.1 Hz.

634 For studying Min patterns on 2D supported lipid bilayer we used a similar protocol for preparation and observing the  
635 Min patterns to the one that was used for the chamber device with a slight modification that SUVs washing was done  
636 manually. In all these experiments we have used SUVs with lipid composition of DOPC:DOPG (67:33) supplemented with  
637 0.03% TopFluor Cardioliolipin.

### 638 **Analysis of the Min Patterns**

639 Analysis of the patterns was done using a self-written Matlab script. For all cases we analyzed the MinE signals, since the  
640 MinD signal gave less contrast and it makes no essential difference since both MinD and MinE signal the same qualitative  
641 and quantitative behavior of the patterns. First, for each movie, the field of view (FOV) was rotated automatically to  
642 make chambers fully vertical by calculating the standard deviation of each line along the average intensity of the movie  
643 and finding the angle at which this value is minimized. Next, the frames of the movies were thresholded using one of  
644 the built-in thresholding methods of Matlab and segmented automatically into chambers by finding intensity steps along  
645 the horizontal and vertical dimensions of an average or STD frame of the movie. We implemented a human-controlled  
646 correction step for both the rotation and segmentation steps in order to bypass program imperfection. The intensity of  
647 the Min proteins in each chamber was then recorded and the average intensity in each chamber was calculated separately  
648 and subtracted in order to produce separate movies for each chamber. The velocity of propagation was calculated by

649 incorporating codes for the U-track 2.1.3 Matlab package that was developed in the Danuser lab [72]. For calculating  
650 the wavelength, a line, featuring the propagating direction was generated automatically based on the U-track results.  
651 Next, the intensity along this line was recorded for each frame of the background subtracted movie and a kymograph  
652 was generated. A peak finder Matlab routine (written by Jacob Kersemakers) was used in order to locate the peaks  
653 distance along each line of the kymograph, and a histogram of the peak distances was generated. A Gaussian fit to the  
654 histogram was then used in order to find the mean value of the wavelength in each chamber. For calculating wavelengths  
655 on flat supported lipid bilayer (SLB), we used the same algorithm with the slight modification that the line along the  
656 waves' propagation direction was drawn manually. Velocities of the wave propagation on 2D flat SLB were calculated by  
657 rotating the peaks' kymograph and minimizing the average standard deviation along each line of the rotated kymograph.  
658 From the angle that minimizes the standard deviation and the error in the angle one can easily infer back the propagation  
659 velocity. Figures and graphs for this article were prepared using the programs: ImageJ (RRID:SCR\_001935), SciDAVis  
660 (RRID:SCR\_014643), Inkscape (RRID:SCR\_014479) and GIMP (RRID:SCR\_003182).

#### 661 **Calculation of the protein concentration in the chambers**

662 Our method of measuring the concentration of the Min proteins is based on the fact that, whereas MinD and MinE  
663 bind the membrane and thus one cannot know their concentration inside the microchambers a priori, the concentration  
664 of a cytosolic protein will always be equal to the concentration that is injected into the device. This means that the  
665 known concentration of a cytosolic fluorescent protein, such as GFP, can be used as a calibration tool in order to infer  
666 the actual concentration of the Min proteins in the microchambers by comparing the relative fluorescence, given that  
667 the relation between the relative fluorescence of GFP and either MinD or MinE is known for conditions where the Min  
668 proteins cannot bind the membrane. Thus, in order to measure the concentrations of the Min proteins in our chambers, we  
669 used a combination of a fluorescent measurement of the Min proteins signal in the chambers relative to their fluorescence  
670 at different concentrations in a cuvette measured with a fluorometer, and compared these values to the fluorescence of  
671 purified green fluorescence protein (deGFP - a variant of GFP see Ref. [73]), which was a kind gift of the Christophe  
672 Danelon lab ( $[C_{GFP}^{Stock}] = 15 \pm 0.9 \mu M$  as measured by the Pierce 660 assay from Thermo Fisher scientific).

673 The concentration of a fluorescence species is related to the signal of a detector ( $S$ ) according to the formula:

$$S = [C] \cdot B \cdot Qeff \cdot I \cdot \tau, \quad (1)$$

674 where  $[C]$  is the concentration of the fluorescent species,  $B$  is the brightness of the species,  $Qeff$  is the quantum efficiency  
 675 of the detector at the emission wavelength of the fluorescent species,  $I$  is the intensity of the light source at the excitation  
 676 wavelength of the fluorescent species, and  $\tau$  is the acquisition time of the detector. Upon defining  $F \equiv Qeff \cdot I \cdot \tau$ , we  
 677 obtain  $S_{Min} = F_{Min} \cdot B_{Min} \cdot [C_{Min}]$  for the Min proteins, and similarly  $S_{GFP} = F_{GFP} \cdot B_{GFP} \cdot [C_{GFP}]$  for GFP. Since  
 678 this equation can be written for both the bulk fluorometer ( $S^{Flu}$ ) and for the microscopic imaging of the chambers ( $S^{Mic}$ )  
 679 one obtains the following two equations:

$$\frac{S_{Min}^{Flu}}{S_{GFP}^{Flu}} = \frac{[C_{Min}^{Flu}] \cdot F_{Min}^{Flu} \cdot B_{Min}}{[C_{GFP}^{Flu}] \cdot F_{GFP}^{Flu} \cdot B_{GFP}}, \quad (2)$$

$$\frac{S_{Min}^{Mic}}{S_{GFP}^{Mic}} = \frac{[C_{Min}^{Mic}] \cdot F_{Min}^{Mic} \cdot B_{Min}}{[C_{GFP}^{Mic}] \cdot F_{GFP}^{Mic} \cdot B_{GFP}}, \quad (3)$$

680 where, for each variable, the superscripts  $Mic$  or  $Flu$  represent the case for the microchamber or the fluorometer cuvette,  
 681 respectively. By defining  $F^{Mic} \equiv \frac{F_{Min}^{Mic}}{F_{GFP}^{Mic}}$  and  $F^{Flu} \equiv \frac{F_{Min}^{Flu}}{F_{GFP}^{Flu}}$  and rearranging eq. (2) and (3), one obtains:

$$[C_{GFP}^{Flu}] = \frac{S_{GFP}^{Flu}}{S_{Min}^{Flu}} \cdot F^{Flu} \cdot \frac{B_{Min}}{B_{GFP}} \cdot [C_{Min}^{Flu}], \quad (4)$$

$$[C_{GFP}^{Mic}] = \frac{S_{GFP}^{Mic}}{S_{Min}^{Mic}} \cdot F^{Mic} \cdot \frac{B_{Min}}{B_{GFP}} \cdot [C_{Min}^{Mic}]. \quad (5)$$

682 Since the GFP concentration is known and the same for the fluorometer and microchambers,  $[C_{GFP}^{Mic}] = [C_{GFP}^{Flu}]$  and we  
 683 can equate eq. 4 and 5 to obtain:

$$[C_{Min}^{Mic}] = [C_{Min}^{Flu}] \cdot \left( \frac{S_{GFP}^{Flu}}{S_{Min}^{Flu}} \cdot \frac{F^{Flu}}{F^{Mic}} \cdot \frac{S_{Min}^{Mic}}{S_{GFP}^{Mic}} \right) \equiv [C_{Min}^{Flu}] \cdot \mathcal{F}. \quad (6)$$

684 Note that  $F^{Mic}$  and  $F^{Flu}$  are pure machine factors, they can be calculated from the known specs of the microscope camera  
 685 and fluorometer detector, the relative intensities of the microscope and fluorometer light sources, and the acquisition times  
 686 in both case.

687 To solve eq. 6 and thus deduce the value of  $C_{Min}^{Mic}$ , one can adapt one out of two strategies that are mathematically  
 688 equivalent. In the first approach, one substitutes all measured  $S$  values to eq. 6, as well as  $[C_{Min}^{Flu}] = [C_{Min}^{Syr}]$ , where

689  $[C_{Min}^{Syr}]$  is the concentration of the Min protein in the syringe that was used in order to inject the Min proteins into  
 690 the microchambers, to thus obtain  $[C_{Min}^{Mic}]$ . In the second strategy, which was in fact applied in our work, we account  
 691 explicitly for the possibly nonlinear dependence of fluorescence intensity versus concentration. Since for varying protein  
 692 concentrations,  $\mathcal{F}$  is a function of  $S_{Min}^{Flu}$ , one can convert the measured  $S_{Min}^{Flu}$  values (see Figure 5 - figure supplement  
 693 1(a),(b)) to values for  $\mathcal{F}$  and read off the value of  $[C_{Min}^{Flu}]$  where  $\mathcal{F}=1$ . At this particular point we thus obtain the  
 694 unknown Min concentration  $[C_{Min}^{Mic}]$  in the microchambers. Note that for MinE, the calibration curve (Figure 5 - figure  
 695 supplement 1(b)) was linear while it was found to be nonlinear for MinD (Figure 5 - figure supplement 1(a)). We do not  
 696 fully understand the source of this non-linearity, but we suspect that is related to some dequenching effect. However, the  
 697 behavior was clearly reproducible as it was repeated in three independent experiments. Note also that the background  
 698 signals in the microchambers in all fluorescence channels were measured before the injection of the proteins and were  
 699 subtracted for the signal in the microchambers in the presence of the proteins. Similarly, the background values in the  
 700 fluorometer were measured and subtracted from the protein signals.

#### 701 **Observation of Min oscillation *in vivo***

702 Strain FW1919 (W3110 [minDE :: exobrs-sfGFP-minD minE-mKate2 :: frt]) [65] was used in order to view Min oscillations  
 703 *in vivo*. Cells were inoculated into LB and were grown overnight at 37°C with 250 rpm shaking. In the morning, the  
 704 cells were diluted 1:100 into M9 media + 0.2% glucose and continued to grow under the same conditions until they  
 705 reached an OD of 0.3. Next, the cells were divided into two fractions. The first fraction was directly transferred to an  
 706 M9 (+0.2% glucose) agar pad and were observed under the microscope to collect movies of Min oscillations in wild type  
 707 cells. Cephalixin, (100  $\mu\text{g/ml}$ , Sigma-Aldrich) was added to the second fraction and the cells continued to grow under  
 708 the same conditions until they reached an OD of 0.94. Then, they were diluted 1 : 3 into fresh M9 +0.2% glucose, placed  
 709 on a similar agar pad, and were observed under the microscope to collect Min oscillations movies in filamentous cells. In  
 710 all cases, movies were taken with the same Olympus IX81 setup that was used for the microchambers experiments. The  
 711 temperature of the microscope was kept at 36.7°C and the acquisition was done using an Olympus UplanApo objective  
 712 (100X, NA 1.35).

713 Movies were analyzed twice. First, to create supplementary file 1(a)-(d) and the corresponding movie, the cells  
 714 boundaries were identified by thresholding and the particle detection tool of ImageJ. Second, the midline of the cells was  
 715 identified using a self-written script in Matlab based on thresholding and discretion of the cell boundaries into two halves

716 (see ref. [74]). The midline was used in order to dissect the cells to separate areas each one with a width of  $0.2 \mu\text{m}$ . The  
717 fluorescence in each area was summed and was used in order to construct the kymographs (supplementary file 1(e)-(h)).

## 718 Acknowledgment

719 This work was supported by the Netherlands Organization for Scientific Research (NWO/OCW), as part of the Frontiers  
720 of Nanoscience program, and the European Research Council for ERC Advanced Grant SynDiv (No. 669598). We would  
721 like to thank Petra Schwille for supplying the Min proteins strains, Christophe Danelon and Pauline van Nies for the kind  
722 gift of the GFP, Jacob Kerssemakers for help with the analysis algorithm, and Fabai Wu, Erwin Frey and Jacob Halatek  
723 for inspiring discussion.

## 724 References

- 725 [1] M. Loose, K. Kruse, P. Schwille, Protein self-organization: lessons from the Min system., *Annu Rev Biophys* 40 (2011)  
726 315–336. doi:10.1146/annurev-biophys-042910-155332.
- 727 [2] J. Lutkenhaus, The ParA/MinD family puts things in their place., *Trends Microbiol* 20 (2012) 411–418. doi:  
728 10.1016/j.tim.2012.05.002.
- 729 [3] Y.-L. Shih, M. Zheng, Spatial control of the cell division site by the Min system in *Escherichia coli*., *Environ Microbiol*  
730 15 (2013) 3229–3239. doi:10.1111/1462-2920.12119.
- 731 [4] V. W. Rowlett, W. Margolin, The Min system and other nucleoid-independent regulators of Z-ring positioning., *Front*  
732 *Microbiol* 6 (2015) 478. doi:10.3389/fmicb.2015.00478.
- 733 [5] D. M. Raskin, P. A. de Boer, Rapid pole-to-pole oscillation of a protein required for directing division to the middle  
734 of *Escherichia coli*., *Proc Natl Acad Sci U S A* 96 (1999) 4971–4976. doi:10.1073/pnas.96.9.4971.
- 735 [6] Z. Hu, J. Lutkenhaus, Topological regulation of cell division in *escherichia coli* involves rapid pole to pole oscillation  
736 of the division inhibitor MinC under the control of MinD and MinE., *Mol Microbiol* 34 (1999) 82–90. doi:10.1046/  
737 j.1365-2958.1999.01575.x.
- 738 [7] C. A. Hale, H. Meinhardt, P. A. de Boer, Dynamic localization cycle of the cell division regulator MinE in *Escherichia*  
739 *coli*., *EMBO J* 20 (2001) 1563–1572. doi:10.1093/emboj/20.7.1563.

- 
- 740 [8] K. Kruse, M. Howard, W. Margolin, An experimentalist's guide to computational modelling of the Min system., Mol  
741 Microbiol 63 (5) (2007) 1279–1284. doi:10.1111/j.1365-2958.2007.05607.x.
- 742 [9] S. Soh, M. Byrska, K. Kandere-Grzybowska, B. A. Grzybowski, Reaction-diffusion systems in intracellular molecular  
743 transport and control., Angew Chem Int Ed Engl 49 (2010) 4170–4198. doi:10.1002/anie.200905513.
- 744 [10] Z. Hu, J. Lutkenhaus, A conserved sequence at the C-terminus of MinD is required for binding to the membrane and  
745 targeting MinC to the septum., Mol Microbiol 47 (2003) 345–355. doi:10.1046/j.1365-2958.2003.03321.x.
- 746 [11] T. H. Szeto, S. L. Rowland, C. L. Habrukowich, G. F. King, The MinD membrane targeting sequence is a trans-  
747 plantable lipid-binding helix., J Biol Chem 278 (2003) 40050–40056. doi:10.1074/jbc.M306876200.
- 748 [12] E. Mileykovskaya, I. Fishov, X. Fu, B. D. Corbin, W. Margolin, W. Dowhan, Effects of phospholipid composition  
749 on MinD-membrane interactions in vitro and in vivo., J Biol Chem 278 (2003) 22193–22198. doi:10.1074/jbc.  
750 M302603200.
- 751 [13] L. D. Renner, D. B. Weibel, MinD and MinE interact with anionic phospholipids and regulate division plane formation  
752 in Escherichia coli., J Biol Chem 287 (2012) 38835–38844. doi:10.1074/jbc.M112.407817.
- 753 [14] P. A. de Boer, R. E. Crossley, A. R. Hand, L. I. Rothfield, The MinD protein is a membrane ATPase required for the  
754 correct placement of the Escherichia coli division site., EMBO J 10 (1991) 4371–4380.
- 755 [15] Z. Hu, J. Lutkenhaus, Topological regulation of cell division in E. coli. spatiotemporal oscillation of MinD requires  
756 stimulation of its ATPase by MinE and phospholipid., Mol Cell 7 (2001) 1337–1343.
- 757 [16] L. L. Lackner, D. M. Raskin, P. A. J. de Boer, ATP-dependent interactions between Escherichia coli Min proteins  
758 and the phospholipid membrane in vitro., J Bacteriol 185 (2003) 735–749. doi:10.1128/jb.185.3.735-749.2003.
- 759 [17] M. Zheng, Y.-L. Chiang, H.-L. Lee, L.-R. Kong, S.-T. D. Hsu, I.-S. Hwang, L. I. Rothfield, Y.-L. Shih, Self-assembly of  
760 MinE on the membrane underlies formation of the MinE ring to sustain function of the Escherichia coli Min system.,  
761 J Biol Chem 289 (2014) 21252–21266. doi:10.1074/jbc.M114.571976.
- 762 [18] L.-Y. Ma, G. King, L. Rothfield, Mapping the MinE site involved in interaction with the MinD division site selection  
763 protein of Escherichia coli., J Bacteriol 185 (2003) 4948–4955. doi:10.1128/jb.185.16.4948-4955.2003.

- 
- 764 [19] Z. Hu, E. P. Gogol, J. Lutkenhaus, Dynamic assembly of MinD on phospholipid vesicles regulated by ATP and MinE.,  
765 Proc Natl Acad Sci U S A 99 (2002) 6761–6766. doi:10.1073/pnas.102059099.
- 766 [20] M. Loose, E. Fischer-Friedrich, C. Herold, K. Kruse, P. Schwille, Min protein patterns emerge from rapid rebinding  
767 and membrane interaction of MinE., Nat Struct Mol Biol 18 (2011) 577–583. doi:10.1038/nsmb.2037.
- 768 [21] K.-T. Park, W. Wu, K. P. Battaile, S. Lovell, T. Holyoak, J. Lutkenhaus, The Min oscillator uses MinD-dependent  
769 conformational changes in MinE to spatially regulate cytokinesis., Cell 146 (2011) 396–407. doi:10.1016/j.cell.  
770 2011.06.042.
- 771 [22] C.-W. Hsieh, T.-Y. Lin, H.-M. Lai, C.-C. Lin, T.-S. Hsieh, Y.-L. Shih, Direct MinE-membrane interaction contributes  
772 to the proper localization of MinDE in *E. coli*., Mol Microbiol 75 (2010) 499–512. doi:10.1111/j.1365-2958.2009.  
773 07006.x.
- 774 [23] Y.-L. Shih, K.-F. Huang, H.-M. Lai, J.-H. Liao, C.-S. Lee, C.-M. Chang, H.-M. Mak, C.-W. Hsieh, C.-C. Lin, The N-  
775 terminal amphipathic helix of the topological specificity factor MinE is associated with shaping membrane curvature.,  
776 PLoS One 6 (2011) e21425. doi:10.1371/journal.pone.0021425.
- 777 [24] Z. Hu, C. Saez, J. Lutkenhaus, Recruitment of MinC, an inhibitor of Z-ring formation, to the membrane in *Escherichia*  
778 *coli*: role of MinD and MinE., J Bacteriol 185 (2003) 196–203. doi:10.1128/jb.185.1.196-203.2003.
- 779 [25] L. Ma, G. F. King, L. Rothfield, Positioning of the MinE binding site on the MinD surface suggests a plausible  
780 mechanism for activation of the *Escherichia coli* MinD ATPase during division site selection., Mol Microbiol 54  
781 (2004) 99–108. doi:10.1111/j.1365-2958.2004.04265.x.
- 782 [26] W. Wu, K.-T. Park, T. Holyoak, J. Lutkenhaus, Determination of the structure of the MinD-ATP complex reveals  
783 the orientation of MinD on the membrane and the relative location of the binding sites for MinE and MinC., Mol  
784 Microbiol 79 (2011) 1515–1528. doi:10.1111/j.1365-2958.2010.07536.x.
- 785 [27] Z. Hu, A. Mukherjee, S. Pichoff, J. Lutkenhaus, The MinC component of the division site selection system in  
786 *Escherichia coli* interacts with FtsZ to prevent polymerization., Proc Natl Acad Sci U S A 96 (1999) 14819–14824.  
787 doi:10.1073/pnas.96.26.14819.

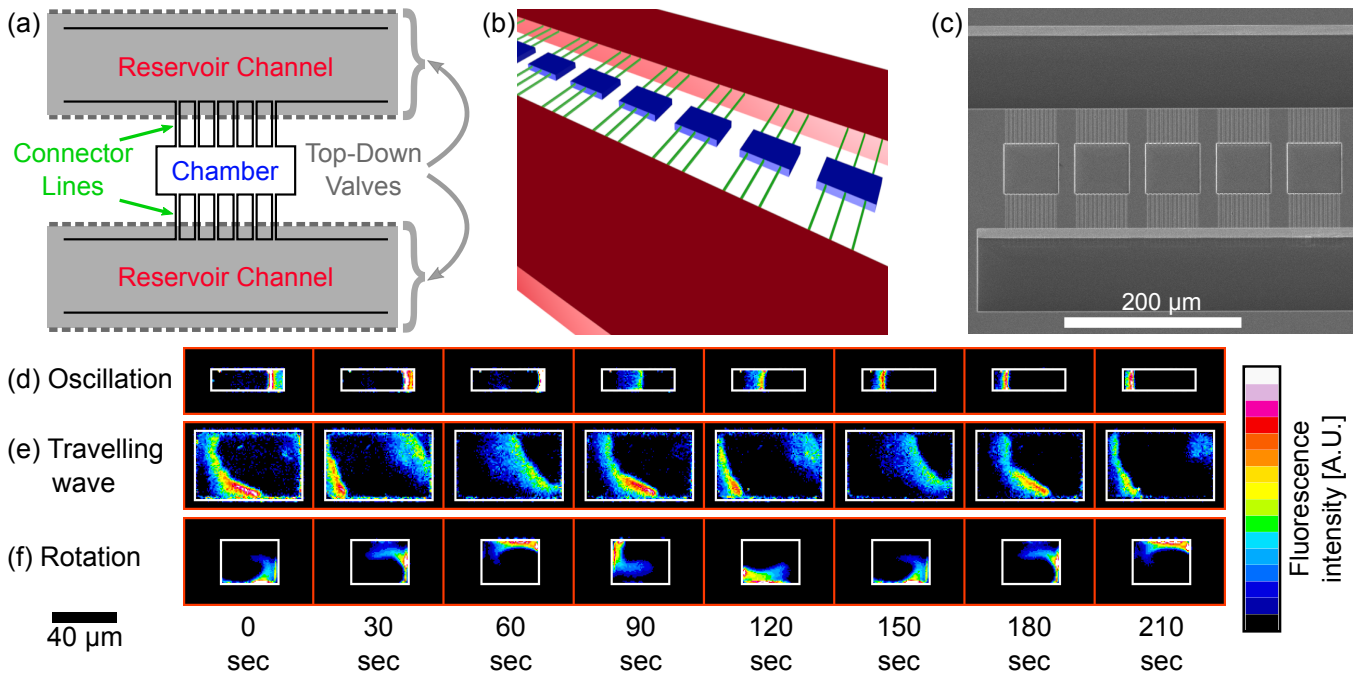
- 
- 788 [28] S. C. Cordell, R. E. Anderson, J. Löwe, Crystal structure of the bacterial cell division inhibitor MinC., *EMBO J* 20  
789 (2001) 2454–2461. doi:10.1093/emboj/20.10.2454.
- [29] A. Dajkovic, A. Mukherjee, J. Lutkenhaus, Investigation of regulation of FtsZ assembly by Sula and development of  
791 a model for FtsZ polymerization., *J Bacteriol* 190 (2008) 2513–2526. doi:10.1128/JB.01612-07.
- [30] A. Touhami, M. Jericho, A. D. Rutenberg, Temperature dependence of MinD oscillation in *Escherichia coli*: running  
793 hot and fast., *J Bacteriol* 188 (2006) 7661–7667. doi:10.1128/JB.00911-06.
- [31] B. D. Corbin, X.-C. Yu, W. Margolin, Exploring intracellular space: function of the Min system in round-shaped  
795 *Escherichia coli*., *EMBO J* 21 (2002) 1998–2008. doi:10.1093/emboj/21.8.1998.
- [32] Y.-L. Shih, I. Kawagishi, L. Rothfield, The MreB and Min cytoskeletal-like systems play independent roles in prokary-  
797 otic polar differentiation., *Mol Microbiol* 58 (2005) 917–928. doi:10.1111/j.1365-2958.2005.04841.x.
- [33] J. Männik, F. Wu, F. J. H. Hol, P. Bisicchia, D. J. Sherratt, J. E. Keymer, C. Dekker, Robustness and accuracy  
799 of cell division in *Escherichia coli* in diverse cell shapes., *Proc Natl Acad Sci U S A* 109 (2012) 6957–6962. doi:  
800 10.1073/pnas.1120854109.
- [34] A. Varma, K. C. Huang, K. D. Young, The Min system as a general cell geometry detection mechanism: branch  
802 lengths in Y-shaped *escherichia coli* cells affect Min oscillation patterns and division dynamics., *J Bacteriol* 190  
803 (2008) 2106–2117. doi:10.1128/JB.00720-07.
- [35] F. Wu, B. G. C. van Schie, J. E. Keymer, C. Dekker, Symmetry and scale orient Min protein patterns in shaped  
805 bacterial sculptures., *Nat Nanotechnol* 10 (2015) 719–726. doi:10.1038/nnano.2015.126.
- [36] M. Loose, E. Fischer-Friedrich, J. Ries, K. Kruse, P. Schwille, Spatial regulators for bacterial cell division self-organize  
807 into surface waves in vitro., *Science* 320 (2008) 789–792. doi:10.1126/science.1154413.
- [37] A. G. Vecchiarelli, M. Li, M. Mizuuchi, C. L. Hwang, Y. Seol, K. C. Neuman, K. Mizuuchi, Membrane-bound MinDE  
808 complex acts as a toggle switch that drives Min oscillation coupled to cytoplasmic depletion of MinD, *Proc Natl Acad*  
809 *Sci U S A* 113 (2016) E1479 – E1488. doi:10.1073/pnas.1600644113.
- [38] J. Schweizer, M. Loose, M. Bonny, K. Kruse, I. Mönch, P. Schwille, Geometry sensing by self-organized protein  
811 patterns., *Proc Natl Acad Sci U S A* 109 (2012) 15283–15288. doi:10.1073/pnas.1206953109.  
812

- 
- 813 [39] K. Zieske, J. Schweizer, P. Schwille, Surface topology assisted alignment of Min protein waves., *FEBS Lett* 588 (2014)  
814 2545–2549. doi:10.1016/j.febslet.2014.06.026.
- 815 [40] K. Zieske, P. Schwille, Reconstitution of pole-to-pole oscillations of Min proteins in microengineered polydimethyl-  
816 siloxane compartments., *Angew Chem Int Ed Engl* 52 (2013) 459–462. doi:10.1002/anie.201207078.
- 817 [41] K. Zieske, P. Schwille, Reconstitution of self-organizing protein gradients as spatial cues in cell-free systems., *Elife* 3  
818 (2014) e03949. doi:10.7554/eLife.03949.
- 819 [42] B. Di Ventura, V. Sourjik, Self-organized partitioning of dynamically localized proteins in bacterial cell division., *Mol*  
820 *Syst Biol* 7 (2011) 457. doi:10.1038/msb.2010.111.
- 821 [43] A. Martos, Z. Petrasek, P. Schwille, Propagation of MinCDE waves on free-standing membranes., *Environ Microbiol*  
822 15 (2013) 3319–3326. doi:10.1111/1462-2920.12295.
- 823 [44] A. G. Vecchiarelli, M. Li, M. Mizuuchi, K. Mizuuchi, Differential affinities of MinD and MinE to anionic phospholipid  
824 influence Min patterning dynamics in vitro., *Mol Microbiol* 93 (2014) 453–463. doi:10.1111/mmi.12669.
- 825 [45] H. Meinhardt, P. A. de Boer, Pattern formation in *Escherichia coli*: a model for the pole-to-pole oscillations of  
826 Min proteins and the localization of the division site., *Proc Natl Acad Sci U S A* 98 (2001) 14202–14207. doi:  
827 10.1073/pnas.251216598.
- 828 [46] K. C. Huang, N. S. Wingreen, Min-protein oscillations in round bacteria., *Phys Biol* 1 (2004) 229–235. doi:10.1088/  
829 1478-3967/1/4/005.
- 830 [47] G. Meacci, K. Kruse, Min-oscillations in *Escherichia coli* induced by interactions of membrane-bound proteins., *Phys*  
831 *Biol* 2 (2005) 89–97. doi:10.1088/1478-3975/2/2/002.
- 832 [48] E. Fischer-Friedrich, R. N. van Yen, K. Kruse, Surface waves of Min-proteins., *Phys Biol* 4 (2007) 38–47. doi:  
833 10.1088/1478-3975/4/1/005.
- 834 [49] S. N. V. Arjunan, M. Tomita, A new multicompartmental reaction-diffusion modeling method links transient  
835 membrane attachment of *E. coli* MinE to E-ring formation., *Syst Synth Biol* 4 (2010) 35–53. doi:10.1007/  
836 s11693-009-9047-2.

- 
- 837 [50] M. Hoffmann, U. S. Schwarz, Oscillations of Min-proteins in micropatterned environments: a three-dimensional  
838 particle-based stochastic simulation approach., *Soft Matter* 10 (2014) 2388–2396. doi:10.1039/c3sm52251b.
- 839 [51] M. Bonny, E. Fischer-Friedrich, M. Loose, P. Schwille, K. Kruse, Membrane binding of MinE allows for a comprehen-  
840 sive description of Min-protein pattern formation., *PLoS Comput Biol* 9 (2013) e1003347. doi:10.1371/journal.  
841 pcbi.1003347.
- 842 [52] K. C. Huang, Y. Meir, N. S. Wingreen, Dynamic structures in *Escherichia coli*: spontaneous formation of MinE rings  
843 and MinD polar zones., *Proc Natl Acad Sci U S A* 100 (2003) 12724–12728. doi:10.1073/pnas.2135445100.
- 844 [53] J. Halatek, E. Frey, Highly canalized MinD transfer and MinE sequestration explain the origin of robust MinCDE-  
845 protein dynamics., *Cell Rep* 1 (2012) 741–752. doi:10.1016/j.celrep.2012.04.005.
- 846 [54] D. Thalmeier, J. Halatek, E. Frey, Geometry-induced protein pattern formation., *Proc Natl Acad Sci U S A* 113  
847 (2016) 548 – 553. doi:10.1073/pnas.1515191113.
- 848 [55] M. A. Unger, H. P. Chou, T. Thorsen, A. Scherer, S. R. Quake, Monolithic microfabricated valves and pumps by  
849 multilayer soft lithography., *Science* 288 (2000) 113–116. doi:10.1126/science.288.5463.113.
- 850 [56] A. A. Brian, H. M. McConnell, Allogeneic stimulation of cytotoxic T cells by supported planar membranes., *Proc*  
851 *Natl Acad Sci U S A* 81 (1984) 6159–6163. doi:10.1073/pnas.81.19.6159.
- 852 [57] R. P. Richter, R. Bérat, A. R. Brisson, Formation of solid-supported lipid bilayers: an integrated view., *Langmuir* 22  
853 (2006) 3497–3505. doi:10.1021/la052687c.
- 854 [58] V. Ivanov, K. Mizuuchi, Multiple modes of interconverting dynamic pattern formation by bacterial cell division  
855 proteins., *Proc Natl Acad Sci U S A* 107 (2010) 8071–8078. doi:10.1073/pnas.0911036107.
- 856 [59] A. Martos, A. Raso, M. Jiménez, Z. Petrášek, G. Rivas, P. Schwille, FtsZ polymers tethered to the membrane by  
857 ZipA are susceptible to spatial regulation by Min waves., *Biophys J* 108 (2015) 2371–2383. doi:10.1016/j.bpj.  
858 2015.03.031.
- 859 [60] I. M. Kuznetsova, K. K. Turoverov, V. N. Uversky, What macromolecular crowding can do to a protein., *Int J Mol*  
860 *Sci* 15 (2014) 23090–23140. doi:10.3390/ijms151223090.

- 
- 861 [61] F. Trovato, V. Tozzini, Diffusion within the cytoplasm: a mesoscale model of interacting macromolecules., *Biophys J*  
862 107 (2014) 2579–2591. doi:10.1016/j.bpj.2014.09.043.
- 863 [62] I. R. Epstein, J. A. Pojman, *An introduction to nonlinear chemical dynamics*, Oxford University press, 1998.
- 864 [63] P. S. Hagan, Spiral waves in reaction-diffusion equations, *SIAM Journal on Applied Mathematics* 42 (1982) 762–786.  
865 doi:10.1137/0142054.
- 866 [64] L. Yang, M. Dolnik, A. M. Zhabotinsky, I. R. Epstein, Pattern formation arising from interactions between turing  
867 and wave instabilities, *The Journal of Chemical Physics* 117 (2002) 7259–7265. doi:10.1063/1.1507110.
- 868 [65] F. Wu, J. Halatek, M. Reiter, E. Kingma, E. Frey, C. Dekker, Multistability and dynamic transitions of intracellular  
869 Min protein patterns., *Mol Syst Biol* 12 (6) (2016) 873. doi:10.15252/msb.20156724.
- 870 [66] Y.-L. Shih, X. Fu, G. F. King, T. Le, L. Rothfield, Division site placement in *E. coli*: mutations that prevent formation  
871 of the MinE ring lead to loss of the normal midcell arrest of growth of polar MinD membrane domains., *EMBO J* 21  
872 (2002) 3347–3357. doi:10.1093/emboj/cdf323.
- 873 [67] O. Sliusarenko, J. Heinritz, T. Emonet, C. Jacobs-Wagner, High-throughput, subpixel precision analysis of bacterial  
874 morphogenesis and intracellular spatio-temporal dynamics., *Mol Microbiol* 80 (2011) 612–627. doi:10.1111/j.  
875 1365-2958.2011.07579.x.
- 876 [68] S. Unai, P. Kanthang, U. Junthon, W. Ngamsaad, W. Triampo, C. Modchang, C. Krittanai, Quantitative analysis of  
877 time-series fluorescence microscopy using a spot tracking method: application to Min protein dynamics, *Biologia* 64  
878 (2009) 27–42. doi:10.2478/s11756-009-0013-y.
- 879 [69] S. Mazor, T. Regev, E. Mileykovskaya, W. Margolin, W. Dowhan, I. Fishov, Mutual effects of MinD-membrane  
880 interaction: I. Changes in the membrane properties induced by MinD binding., *Biochim Biophys Acta* 1778 (2008)  
881 2496–2504. doi:10.1016/j.bbamem.2008.08.003.
- 882 [70] H.-L. Lee, I.-C. Chiang, S.-Y. Liang, D.-Y. Lee, G.-D. Chang, K.-Y. Wang, S.-Y. Lin, Y.-L. Shih, Quantitative  
883 proteomics analysis reveals the Min system of *Escherichia coli* modulates reversible protein association with the inner  
884 membrane., *Mol Cell Proteomics* 15 (2016) 1572–1583. doi:10.1074/mcp.M115.053603.

- 
- 885 [71] A. Edelstein, N. Amodaj, K. Hoover, R. Vale, N. Stuurman, Computer control of microscopes using  $\mu$ Manager., Curr  
886 Protoc Mol Biol Chapter 14 (2010) Unit14.20. doi:10.1002/0471142727.mb1420s92.
- 887 [72] K. Jaqaman, D. Loerke, M. Mettlen, H. Kuwata, S. Grinstein, S. L. Schmid, G. Danuser, Robust single-particle  
888 tracking in live-cell time-lapse sequences., Nat Methods 5 (8) (2008) 695–702. doi:10.1038/nmeth.1237.
- 889 [73] J. Shin, V. Noireaux, An E. coli cell-free expression toolbox: application to synthetic gene circuits and artificial cells.,  
890 ACS Synth Biol 1 (1) (2012) 29–41. doi:10.1021/sb200016s.
- 891 [74] Y. Caspi, Deformation of filamentous Escherichia coli cells in a microfluidic device: a new technique to study cell  
892 mechanics., PLoS One 9 (1) (2014) e83775. doi:10.1371/journal.pone.0083775.

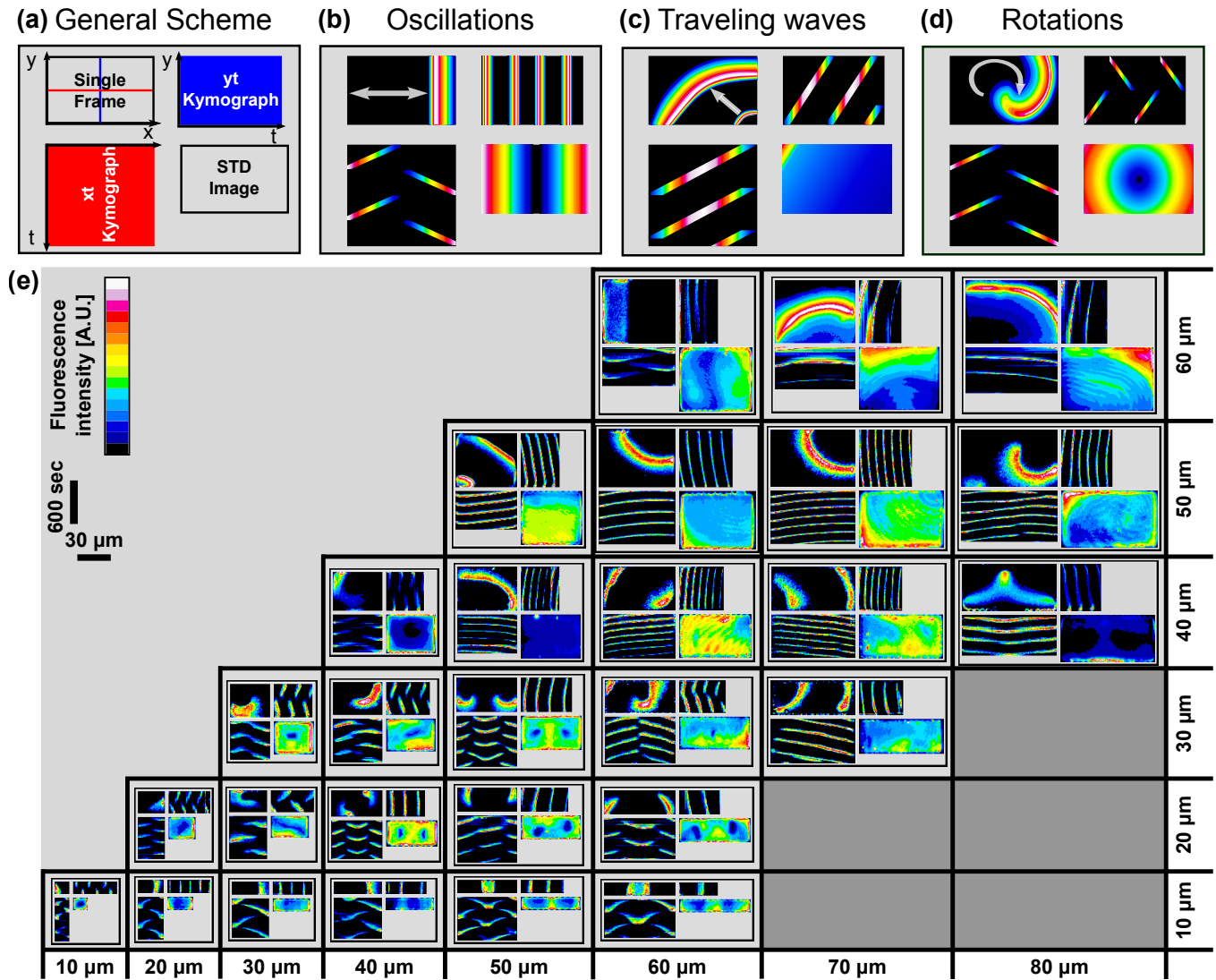
893 **Figures**

894

895 Figure 1: (a) Top view illustration of the microfluidic device structure. We study Min protein pattern formation in  
 896 totally enclosed microfluidic chambers. Each chamber (blue) is  $2.4 \mu m$  high with a width ranging from 10 to  $60 \mu m$  and  
 897 a length ranging from 10 to  $90 \mu m$ . Each chamber is connected through small connector lines (green, with a cross-section  
 898 of  $\sim 0.9 \times 0.9 \mu m$ ) from both sides to two  $\sim 30 \mu m$  deep reservoir channels (red). A top layer of pressurized microfluidic  
 899 valves (gray shading) are placed above the reservoir channels. After the walls of the chambers are coated with a lipid  
 900 bilayer, MinD and MinE proteins are injected into the device. Subsequently, the valves above the reservoir channels are  
 901 closed. Consequently, the rectangular chambers (including the connector lines) are separated from the rest of the device.  
 902 This unique structure allows studying the 3D geometric selection rules of the Min system *in vitro*. (b) 3D illustration of  
 903 the microfluidic device structure. Chambers are in blue, connector lines in green, and reservoir channels in red. For clarity,  
 904 the pressure valves are not shown. (c) SEM image of the silicon wafer master that was used in order to replicate the

---

905 chambers, connector lines and reservoir channels into PDMS. Note that the fabrication was done with a positive resist and,  
906 thus, we have used a double replica method in order to recover the right orientation of the chambers (see Materials and  
907 Methods). (d-f) Characterization of dynamical Min patterns observed in the confined fluidic chambers. (d) Oscillations  
908 - Min proteins periodically move back and forth between two poles of the chamber. (e) Traveling waves - Min proteins  
909 continuously propagate wave fronts from one side zone of the chamber to the other. (f) Rotations - Min zone circulates  
910 around a fixed point in the chamber. Scale bar  $40 \mu m$  applied to all three examples (d-f). Fluorescence signals represent  
911 MinE patterns.

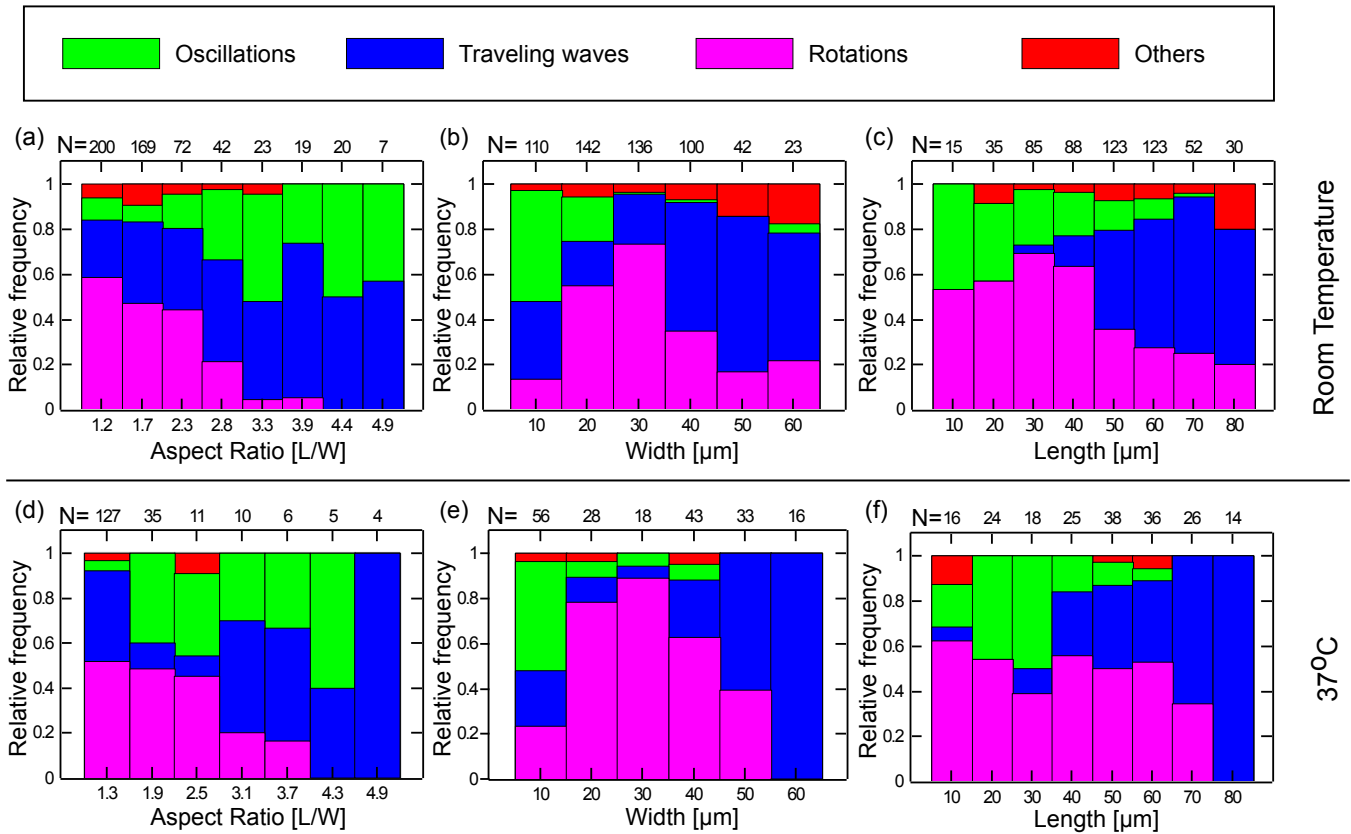


912

913 Figure 2: Atlas of the Min system behavior in 3D confined chambers. We represent the dynamical Min behavior in  
 914 each case as a quadrant. (a) Illustration of the quadrant scheme. Each quadrant is composed of (upper left) A single  
 915 frame from a movie that captures the behavior of the Min system in a specific chamber at a specific point of time; (lower  
 916 right) A temporal standard deviation picture of the movie; (lower left) an Xt-kymograph of the middle line cross-section

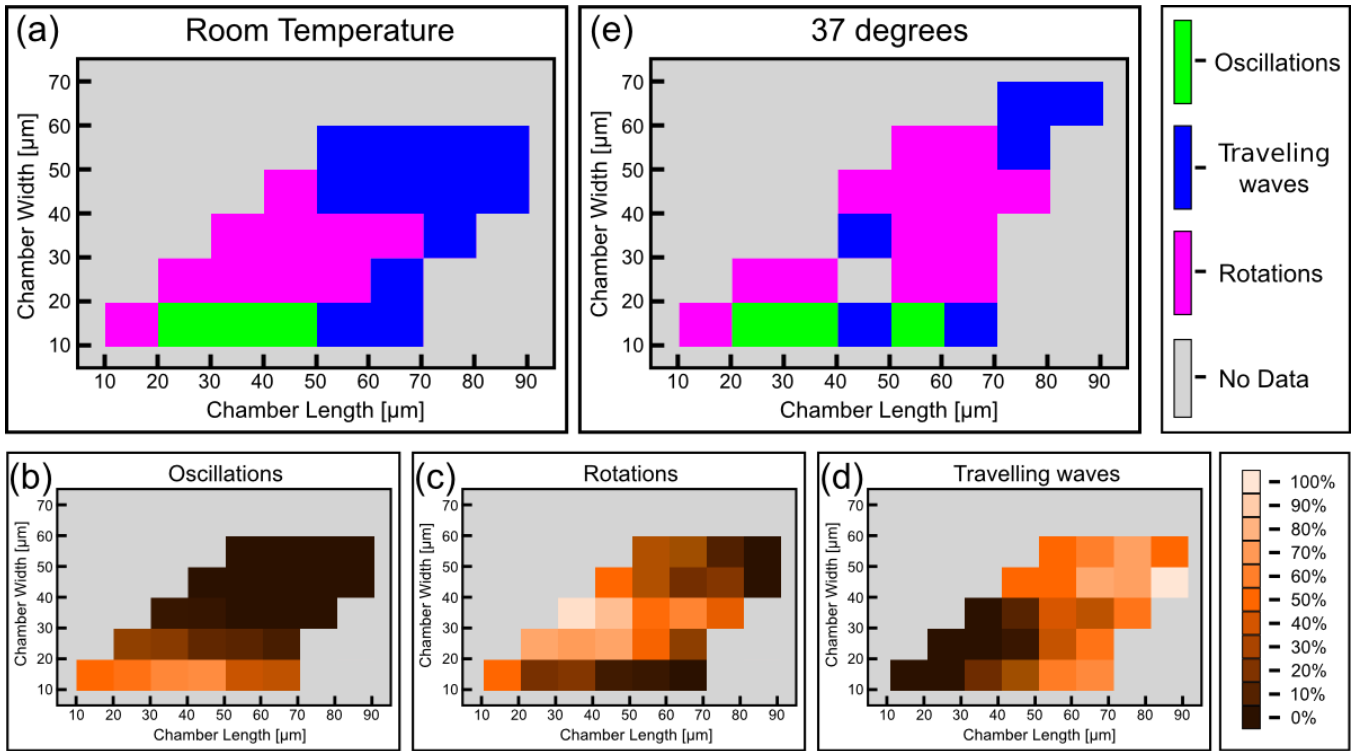
---

of the chamber along the red line in the upper left movie frame image, and (upper right) a  $Yt$ -kymograph of a middle line cross-section of the chamber along the blue line in the upper left movie frame image. (b)-(d) Illustrative examples of the three pure genera of Min dynamics that were observed. (b) Oscillations. (c) Traveling waves, and (d) Rotations. (e) Table representing real examples of observed Min dynamics in the chambers, organized according to the quadrant scheme. Each image is color coded in a 16-colors look-up table as shown in the legend. Scale bar represents  $30 \mu m$  in the  $x$  and  $y$  directions and 600 seconds for the  $Xt$  and  $Yt$  kymographs. A detailed explanation for the quadrant representation of the Min pure and non-pure behaviors is found in the main text. Fluorescence signals represent MinE patterns.



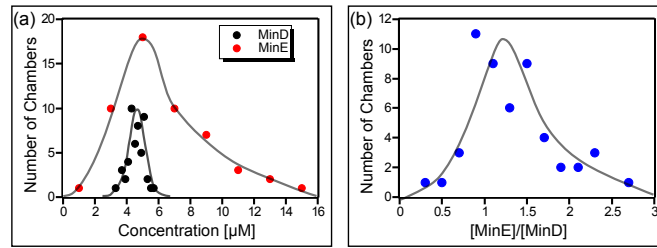
924

925 Figure 3: Preferred dynamical Min behavior as a function of the chamber-geometry parameters. (a)-(c) Geometry  
 926 selection at room temperature. (a) Selection according to the chamber aspect ratio. (b) Selection according to cham-  
 927 ber width. (c) Selection according to chamber length. All measurements were performed at room temperature on a  
 928 DOPC:DOPG (67:33) SLB supplemented with 0.03 of TopFluor Cardiolipin. The number of chambers observed with  
 929 the specific geometrical characteristics are indicated above each bar. (d)-(f) Same as (a)-(c) for measurements that were  
 930 performed at 37°C on an *E. coli* polar lipid extract SLB. The analysis is based on the fluorescence signals of MinE.



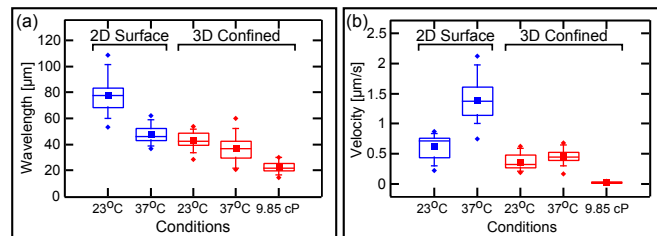
931

932 Figure 4: Phase Diagram of the Min patterns. (a) Phase diagram of the Min behavior at room temperature. Each  
 933 square represents the most abundant behavior in that geometry. Color code is shown on the right. (b)-(d) Relative  
 934 abundance of the pole-to-pole oscillations, rotations and traveling waves in each chamber size. Color code for (b)-(d) is  
 935 shown on the right. (e) Phase diagram of Min behavior at 37°C. Color code is the same as in (a). The analysis is based  
 936 on the fluorescence signals of MinE.



937

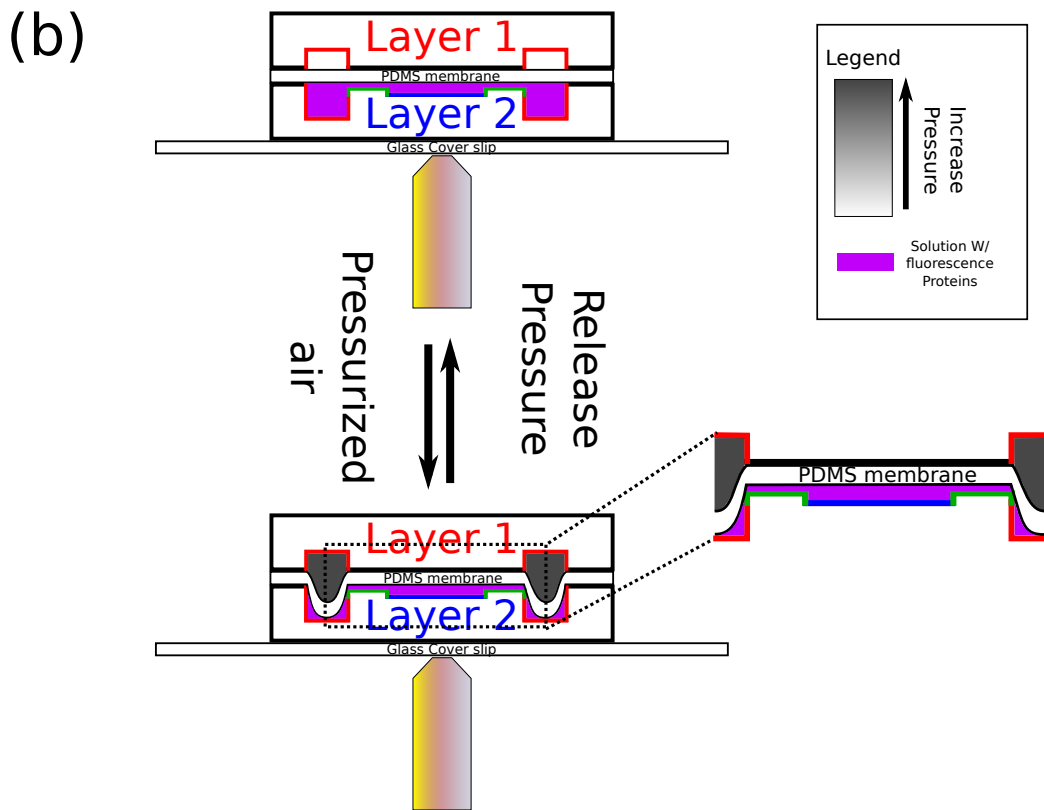
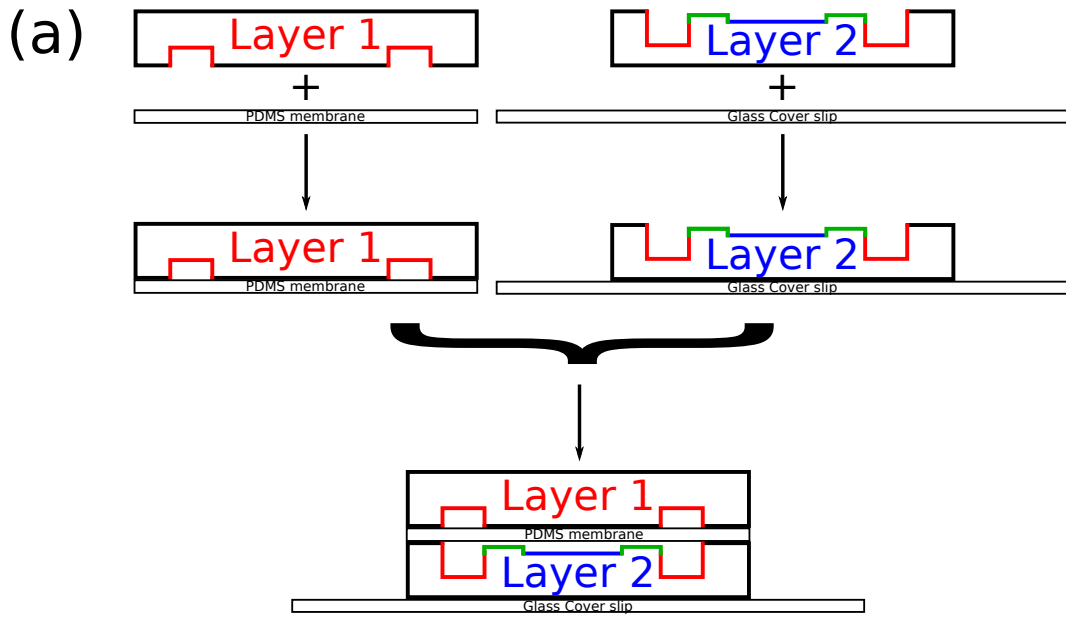
938 Figure 5: (a) Histogram of the deduced concentration of MinE and MinD in the chambers. (b) Idem for the ratio of  
 939 MinE to MinD. Lines are guides to the eye. Concentration was measured using a GFP protein as a standard as described  
 940 in the Materials and Methods.



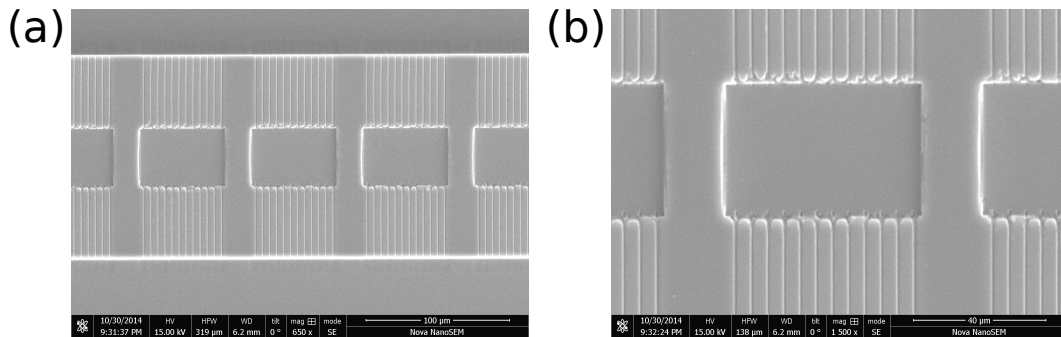
941

942 Figure 6: (a) Statistical box plot representing the wavelength of the Min waves at different conditions: at room  
 943 temperature and at  $37^\circ\text{C}$ , and at flat SLB (blue) as well as inside the 3D confined chambers (red), and with high viscous  
 944 medium in the chambers (at room temperature). The lines of each box represent the location of the 25, 50 and 75  
 945 percentiles. Full squares represent the location of the mathematical mean. Whiskers represent the 5 – 95 percentile range  
 946 and the diamonds the minimum and maximum values of the data. (b) Velocity of Min pattern propagation at the same  
 947 conditions. Box representation is the same as in (a). The analysis is based on the fluorescence signals of MinE.

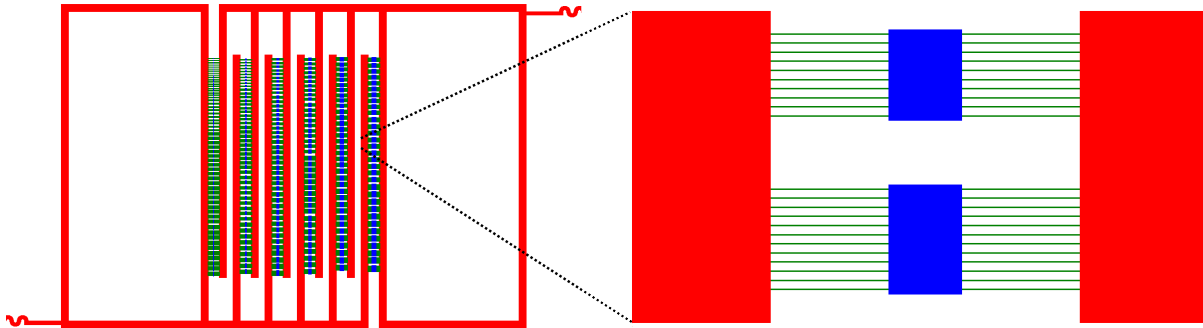
948 **Supporting Figures**



949 Figure 1 - figure supplement 1: (a) Illustration of the fabrication process of the microfluidic device. First, a top layer  
 950 PDMS chip is bound to a thin PDMS membrane via plasma treatment and a high-temperature baking. Next, a lower  
 951 layer PDMS chip with the chambers is bound to a glass coverslip in the same way. Finally, the two parts are aligned and  
 952 bound to each other in the same way. (b) An illustration of the operation of the chip in order to obtain closed microfluidic  
 953 chambers. First, the chip is coated with a supported lipid bilayer. Next, Min proteins are infused in the chambers. Finally,  
 954 the upper layer valves are pressurized with air. As results, one can study the behavior of the Min proteins in confined  
 955 isolated fluidic volumes.

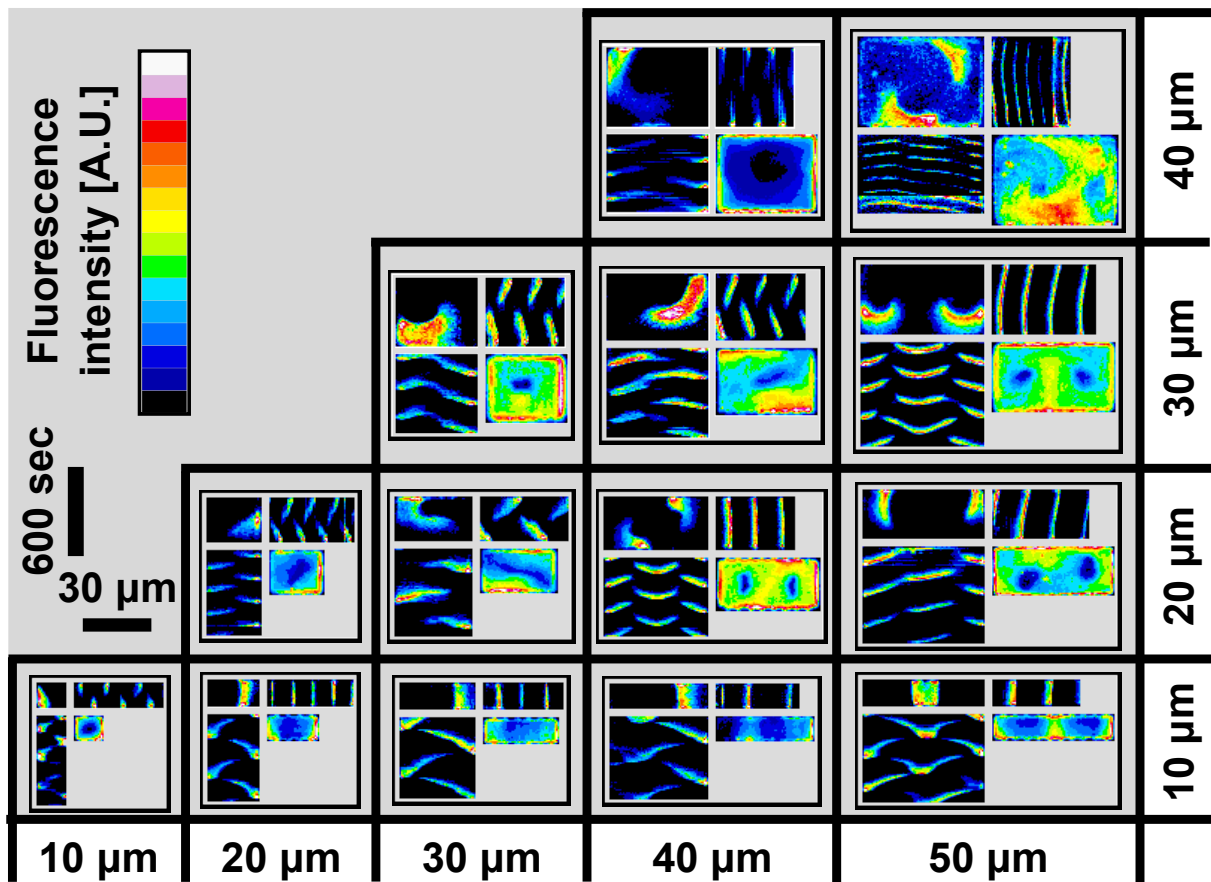


956 Figure 1 - figure supplement 2: SEM images of two different areas in the lower layer PDMS chip.



957 Figure 1 - figure supplement 3: Schematic representation of the overall lower layer chip structure. A series of three  
 958 dimensional closed rectangle chambers. Chambers and lines are in blue. Connector lines are in green, and deep reservoirs

959 channels are in red.

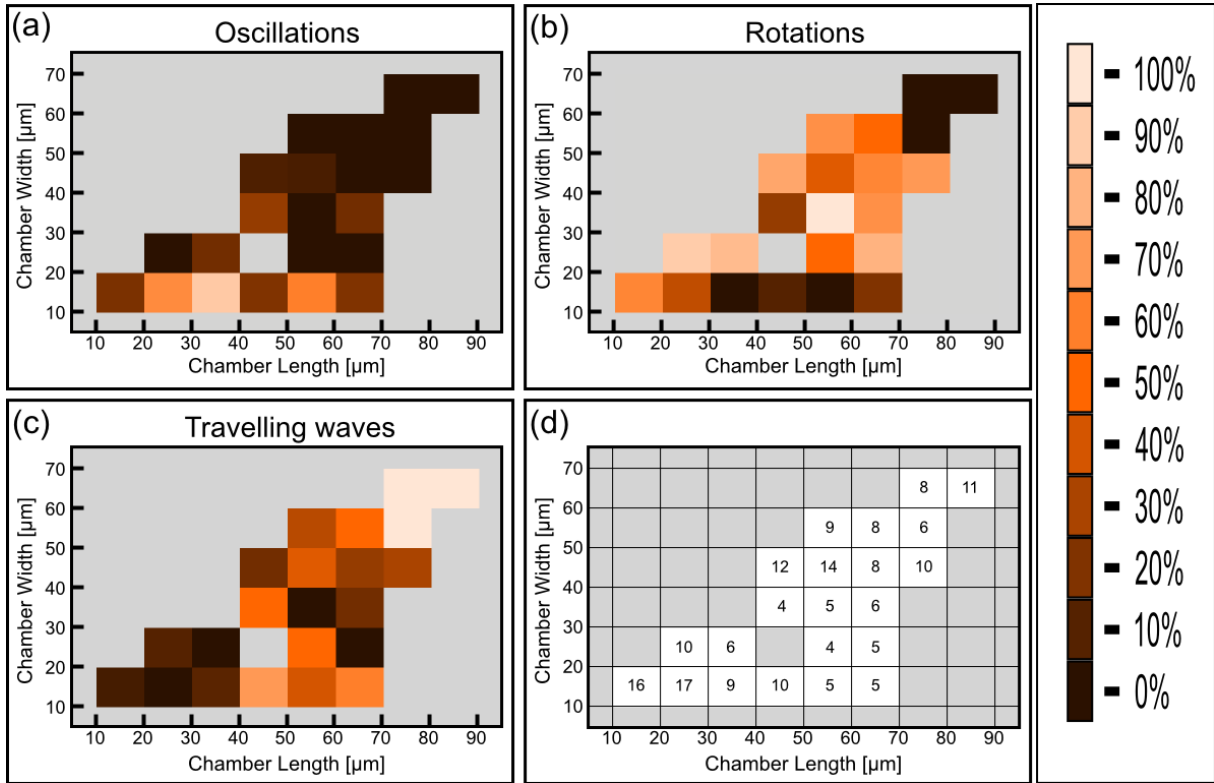


960 Figure 2 - figure supplement 1: An atlas of the Min system behavior in 3D confined chambers. This figure represents  
 961 a zoom of Fig. 2(e). Typical examples of the Min protein behavior in smaller chambers are thus shown at larger  
 962 magnification for clarity. The format of figure follows the same quadrant representation. For more details see the main  
 963 text. Fluorescence signals represent MinE patterns.



967

Figure 4 - figure supplement 1: Number of chambers that were used per each tile for constructing Fig. 4(a)-(d).



968

Figure 4 - figure supplement 2: Detailed analysis of the phase diagram at elevated temperature (Figure corresponding

969

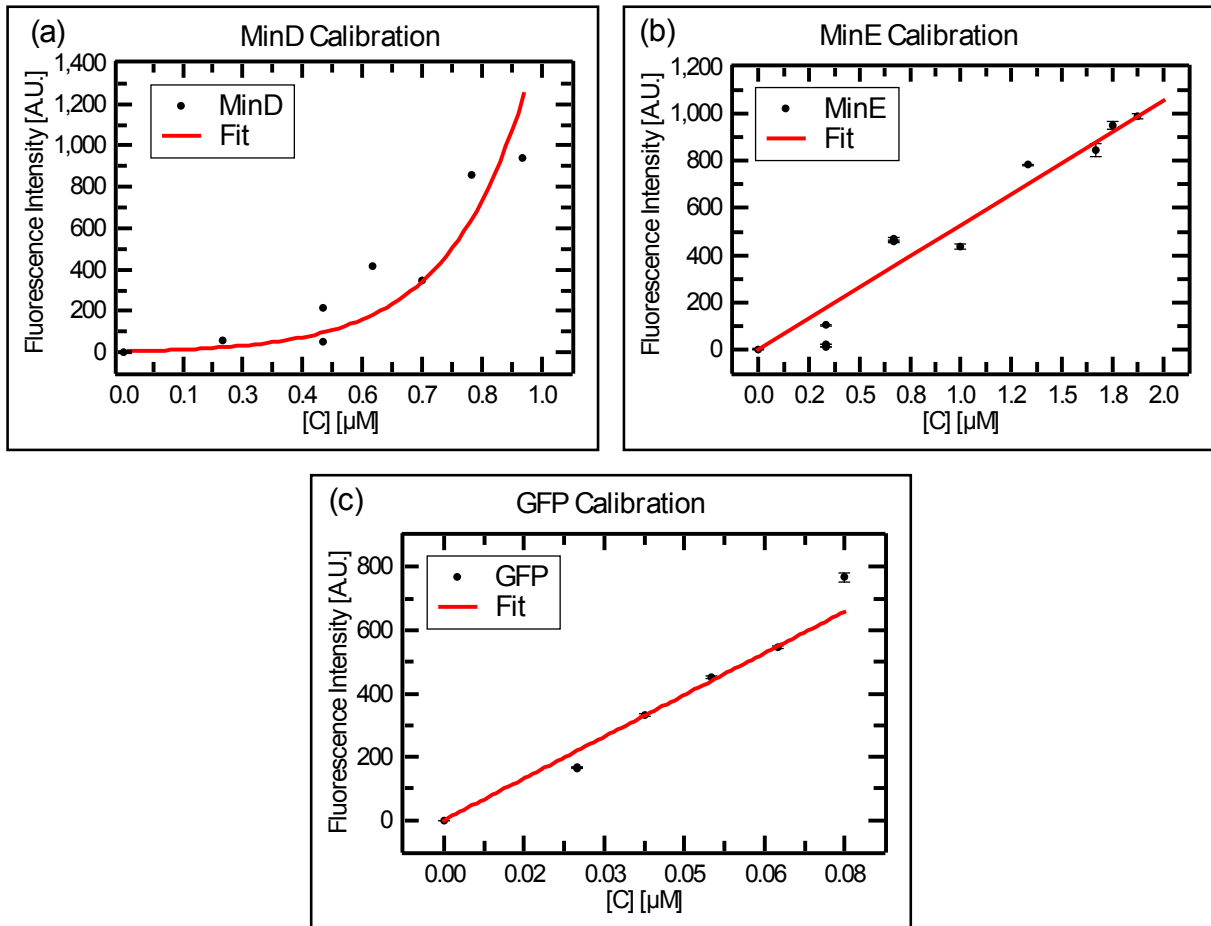
to Fig. 4(e)). (a) Relative abundance of the oscillatory behavior for each chamber size. Color code is defined in the legend

970

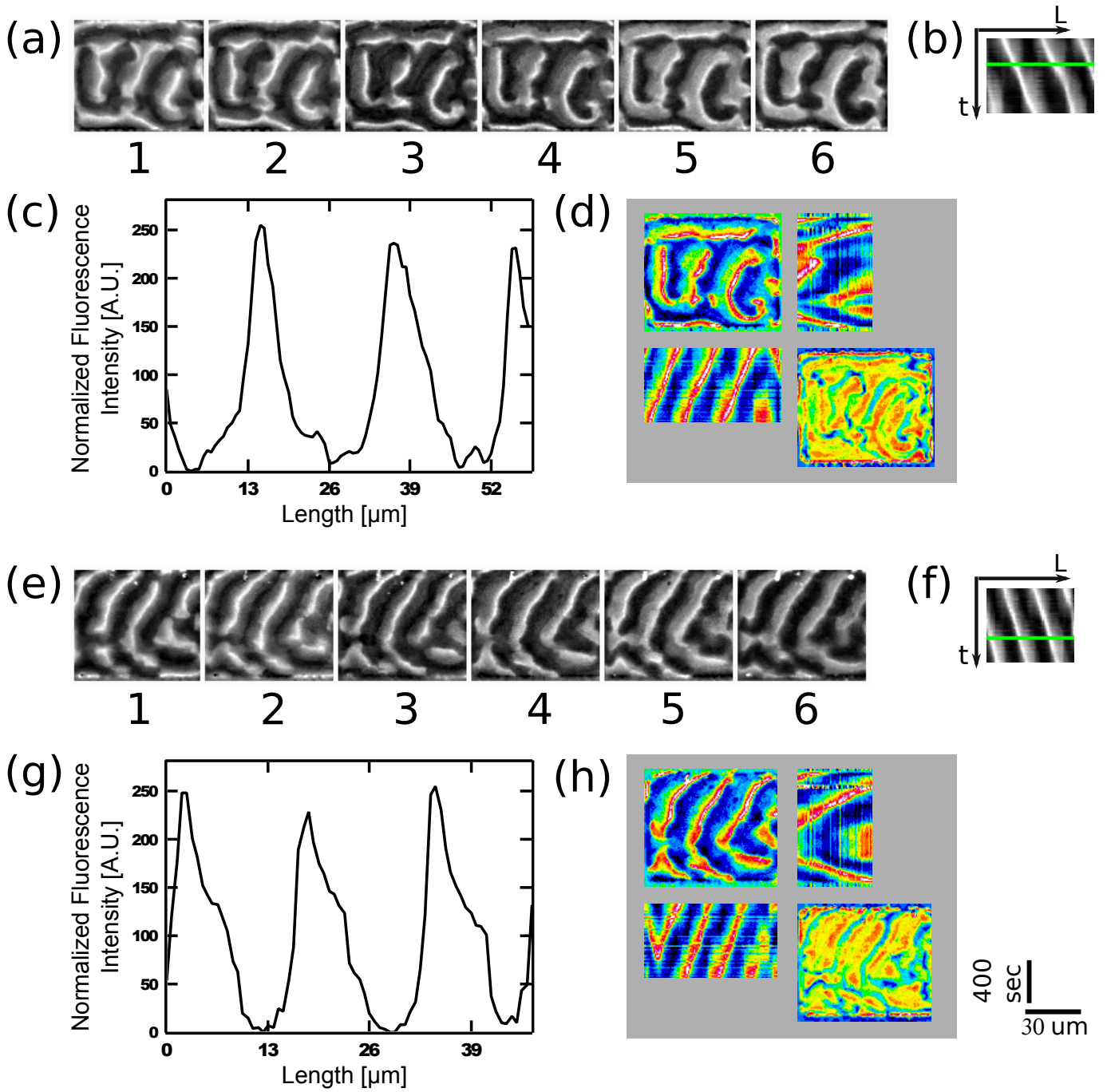
to the right. (b) Same as (a) for rotations. (c) Same as (a) for traveling waves. (d) Number of chambers that were used

971

per each tile for constructing Fig. 4(e) and panels (a)-(c).



972 Figure 5 - figure supplement 1: Calibration curves for the fluorescence intensity of (a) MinD, (b) MinE, and (c) GFP,  
973 as collected with a fluorometer. Stock solution of MinD-Cy3 ( $14 \mu\text{M}$ ) or MinE-Cy5 ( $25 \mu\text{M}$ ) were diluted at various  
974 values and the resulted fluorescence was recorded on a Carry eclipse fluorometer. The same procedure was repeated for  
975 GFP.



976 Figure 6 - figure supplement 1: Examples of traveling waves in the chambers in the presence of a viscous media at  
977 9.85 *cP*. MinD ( $1.1 \mu M$ ), MinE ( $1 \mu M$ ), ATP ( $5 mM$ ) together with an ATP-regeneration system in a crowding solution  
978 (4% BSA, 4% PEG8000 and 4% Ficoll 400) were injected into the chamber device. The panels show the MinE fluorescence  
979 signal. (a) and (e) Montage of the MinE signal in two chambers. Time difference between frames is 60 seconds. In  
980 order to calculate the wavelength, a self-written Matlab code was used (see materials and methods section). A line was  
981 drawn manually along the wave propagation direction and the fluorescence intensity along this line was recorded and  
982 normalized for each frame. (b) and (f) Corresponding kymographs for (a) and (e) that were used in order to calculate  
983 the wavelength and the wave velocity. Wavelength was calculated by fitting a Gaussian function to the distribution of  
984 distances between the intensity peaks of these kymographs. Velocity was calculated based on the angle of the intensity  
985 peaks along the kymographs temporal direction. Wavelengths are equal to  $20 \pm 3 \mu m$  and  $18 \pm 0.7 \mu m$  for (a) and (e)  
986 respectively. Velocities are equal to  $0.021 \pm 0.001 \mu m/sec$  and  $0.024 \pm 0.001 \mu m/sec$  for (a) and (e) respectively. (c)  
987 and (g) Normalized fluorescence intensity along the green line in panels (b) and (f) respectively. (d) and (h) Quadrant  
988 representation on the Min behavior in these two chambers. Format of the representation is similar to the one in Fig. 2(e).  
989 Scale bars for all panels ( $30 \mu m$  and 400 sec) are shown on the bottom right.

990

---

## 991 Captions for supporting movies

992 **Movie 1:** Isolation of 3D confined chambers from the rest of the chip. After the SLB was formed in the device, as  
993 described in the Materials and Methods, the chip was connected to a syringe pump containing Min buffer. A flow of  
994  $75 - 150 \mu\text{m}/\text{h}$  was applied (green traffic light). The application of buffer flow resulted in migration of the SUVs that  
995 did not splash during the previous incubation period on the chambers walls along the stream lines. After  $\sim 3$  minutes  
996 the valves were closed and the flow was stopped (red traffic light). This resulted in an immediate halt of the SUVs flow,  
997 showing that the chambers were isolated from the rest of the chip. In order to show reversibility of the valves operation,  
998 after additional  $\sim 1.5$  minute, the valves were opened (second round of green traffic light). Immediately upon releasing  
999 the pressure in the pressure valves, the SUVs started to flow again, showing that the halting of the flow was the result of  
1000 the valves operation and did not result from, say, stopping the syringe pump operation. Of course, stopping the operation  
1001 of the syringe pump will also result in a stop of the flow in the microfluidic device. However, due to pressure-difference  
1002 equilibration, this process usually lasts couple of minutes. In contrast, upon operating the valves, an immediate stop in  
1003 the flow was observed.

1004 **Movie 2:** Movies of Min patterns formation in chambers with different sizes that were used for the construction of Figure  
1005 2(e) of the main text.

1006 **Movie 3:** Examples of Min oscillations in vivo in strain BN1919 (see Wu et al. (2016) Mol Sys Biol 12: 873). Movie  
1007 corresponds to Supplementary file 1. Fluorescence signal represents MinD oscillations.

1008

---

**1009** **Caption for supplementary file 1**

**1010** **Supplementary file 1:** Examples of *in vivo* oscillations in live cells. (a)-(d) Four examples of *in vivo* MinD oscillations  
**1011** in cells with various length of strain FW1919 (see Wu et al. (2016) Mol Sys Biol 12: 873). Panels show montages of the  
**1012** corresponding supporting movie 3. Time difference between frames is 12 *sec*. Scale bar (5  $\mu m$ ) is shown to the left of panel  
**1013** (d). Cell boundaries are marked in white. (a) Pole-to-pole oscillations in a wild type cell of normal length (3.8  $\mu m$ ). (b)  
**1014** A triple-node oscillations in a Cephalaxin-division-inhibited cell with a length of 11.9  $\mu m$ . (c) Multiple-node oscillations  
**1015** in a Cephalaxin-division-inhibited cell (19.9  $\mu m$ ). (d) Aberrant triple-node oscillations in a Cephalaxin-division-inhibited  
**1016** cell (14.4  $\mu m$ ). For the last case, instead of the regular pattern, where triple-point-oscillations occur between a middle  
**1017** zone and the two poles (see panels (b) and (f)), the middle zone seems to originate in the center of the cell and while  
**1018** traveling toward one pole, a MinD zone is established on the opposite pole. (e)-(h) Corresponding kymographs of the  
**1019** MinD intensity along the cells' length for panels (a)-(d) respectively. Scale bars for the kymographs are shown next to  
**1020** panel (h).